Magmatic fluids responsible for lode gold mineralization in the giant Linglong deposit at Jiaodong, North China Craton: Constraints from Li—O isotopes

Shao-Rui Zhao [a,b], Zhan-Ke Li [a,b,*], Zu-Wei Lin [b], Jian-Feng Gao [c], Hua-Shan Sun [b], Martin Yan Hei Li [d], Xin-Fu Zhao [a,b,*]

[a] State Key Laboratory of Geological Processes and Mineral Resources, China University of Geosciences, Wuhan 430074, China
[b] School of Earth Resources, China University of Geosciences, Wuhan 430074, China
[c] State Key Laboratory of Ore Deposit Geochemistry, Institute of Geochemistry, Chinese Academy of Sciences, Guiyang 550081, China
[d] Department of Earth Sciences, University of Hong Kong, Pokfulam Road, Hong Kong

ARTICLE INFO

ABSTRACT

The Jiaodong Peninsula, located in the eastern margin of the North China Craton, contains numerous world-class lode gold deposits that combined have a proven gold reserve of >5000 t. Despite a large amount of research, the source and evolution of hydrothermal fluids responsible for the gold mineralization in this region remains highly debated. The Linglong gold deposit is one of the largest deposits in the Jiaodong Peninsula. Gold lodes at Linglong are predominantly hosted within the Late Jurassic Linglong granite and structurally controlled by NE-trending faults. They are closely associated with large-scale hydrothermal alteration, which is paragenetically characterized by hydrothermal K-feldspar in pre-ore stage I, and sericite-quartz-pyrite in *syn*-ore stages II and III. The syn-ore alteration mineral assemblage is distributed within and around the gold lodes, whereas the K-feldspar alteration remains mainly distal to the gold lodes. From the unaltered to progressively intensifying K-feldspar-altered Linglong granites, there are decreasing trends for both whole-rock Li concentrations and δ^7Li values, which are attributed to Rayleigh fractionation. The two values increase covariantly within the sericite-quartz-pyrite alteration zone towards the mineralization center, suggesting that further fluid-rock interaction and buffering of the ore fluid accounts for the observed Li elemental and isotopic variations. Fluid inclusion assemblages in quartz of stages I-III have homogenization temperatures of 349°-312 °C, 318°-272 °C, and 307°-246 °C, respectively. In-situ oxygen isotopic analysis on stage I quartz reveals $\delta^{18}O_Q$ values of 10.9–14.7 ‰, corresponding to $\delta^{18}O_W$ values of 4.3–9.2 ‰ for the equilibrated fluid. The $\delta^{18}O_W$ values of the equilibrated fluids of stages II and III are 5.6–8.9 ‰ and 5.2–8.8 ‰, respectively. The oxygen isotopic compositions indicate that magmatic fluid is prevailing for the K-feldspar and sericite-quartz-pyrite alterations. A binary mixing model using Li concentrations and δ^7Li values further implies that the hydrothermal fluid was mainly sourced from coeval mafic magmas derived from the metasomatized lithospheric mantle. Our study highlights that lithium and in-situ oxygen isotopes can be used effectively to fingerprint the source of hydrothermal fluids and fluid-rock interactions.

1. Introduction

Lode gold deposits are an important source of gold, accounting for one-third of the world's resources (Frimmel, 2008). They typically comprise quartz-sulfide veins and/or auriferous altered rocks (Goldfarb et al., 2005). Conventionally, metamorphic fluids formed by devolatilization of fertile sedimentary and/or volcanic rocks during greenschist-to amphibolite-facies metamorphism have been considered to be responsible for the formation of lode gold deposits (Groves et al., 1998; Large et al., 2011; Steadman and Large, 2016; Patten et al., 2020; Pitcairn et al., 2021). Recently, alternative models propose the devolatilization of subducted oceanic plates and the overlying sediments (Goldfarb et al., 2007; Groves et al., 2020) or of a metasomatized mantle lithosphere (Deng et al., 2020a; Wang et al., 2022b) to explain the

genesis of these deposits. Whilst others have augured that magmatic fluids have significantly contributed to generate these gold deposits (e. g., Burrows et al., 1986; Xavier and Foster, 1999; Xue et al., 2013a; Fan et al., 2022).

Isotopes have been shown to be powerful in tracking the origin and evolution of ore fluids. Previous studies on the source and evolution of gold-forming fluids largely relied on quartz H—O isotopes using bulk-sample analysis. This technique, however, would mix the isotopic signatures of multiple paragenetic stages recorded in quartz and thus is problematic in fingerprinting the source and evolution of ore-forming fluids for lode gold deposits (e.g., Fekete et al., 2016; Li et al., 2018b). With the advancement of high-spatial-resolution analytical methods, in-situ oxygen isotopic analysis of quartz has been successfully used to unravel the complex fluid incursion and evolution associated with various hydrothermal deposits (e.g., Tanner et al., 2013; Haroldson et al., 2020; Gao et al., 2021). In addition to oxygen isotopes, lithium isotopes are also powerful in tracing the hydrothermal processes and fingerprinting the fluid sources (e.g., Bernal et al., 2014; Li et al., 2018a; Lu et al., 2021; Nadeau et al., 2021; Xu et al., 2021; Romer et al., 2022) as significant mass fractionation occurs during fluid mobilization of the two isotopes (~17‰) of Li (^{6}Li and ^{7}Li). In contrast, there is very little Li isotopic fractionation in igneous processes of partial melting, fractional crystallization, and fluid exsolution (e.g., Tomascak et al., 1999; Tang et al., 2009; Schuessler et al., 2009; Li et al., 2018a). Although in-situ lithium isotopic analysis has been developed for many years, which are mainly applied for silicate and carbonate minerals with high lithium contents (>2 µg/g; e.g., Vigier et al., 2007; Marks et al., 2008; Martin

et al., 2015; Steinmann et al., 2019; Hoover et al., 2021) and not suitable for low-lithium minerals such as quartz and pyrite. As such, it is difficult to obtain the lithium isotopic compositions of altered rocks by in-situ methods right now.

In this study, we conducted bulk-rock lithium and in-situ quartz oxygen isotopic research on a typical lode gold deposit, the giant Linglong deposit at the Jiaodong Peninsula, China. Our results show that both the mineralization related, pre-gold K-feldspar alteration and syn-gold sericite-quartz-pyrite alteration in this deposit were formed by a magmatic fluid that was dominantly sourced from the metasomatized lithospheric mantle-derived mafic magmas.

2. Geological setting

The Jiaodong Peninsula, situated in the eastern margin of the NCC, is separated by the NE-trending Wulian-Jimo Fault against the Jiaobei Terrane to the northwest and the Sulu ultrahigh-pressure metamorphic belt to the southeast (Fig. 1). The Jiaobei Terrane can be further divided into the Jiaobei Uplift and Jiaolai Basin. The Jiaobei Uplift is situated in the north of the Jiaobei Terrane and is dominated by Neoarchean to Neoproterozoic metamorphic rocks, such as the Jiaodong, Jingshan, Fenzishan, and Penglai groups. These metamorphic rocks were cross-cut by Late Triassic, Late Jurassic, and Early Cretaceous granites (Fig. 1; Chen et al., 2003; Yang et al., 2005; Wang et al., 2014; Li et al., 2019). The Jiaolai Basin in the south of the Jiaobei Terrane is dominated by Cretaceous sedimentary-volcanic rocks (Fig. 1; Xie et al., 2012). The Jiaodong Peninsula is structurally characterized by a number of NNE- to
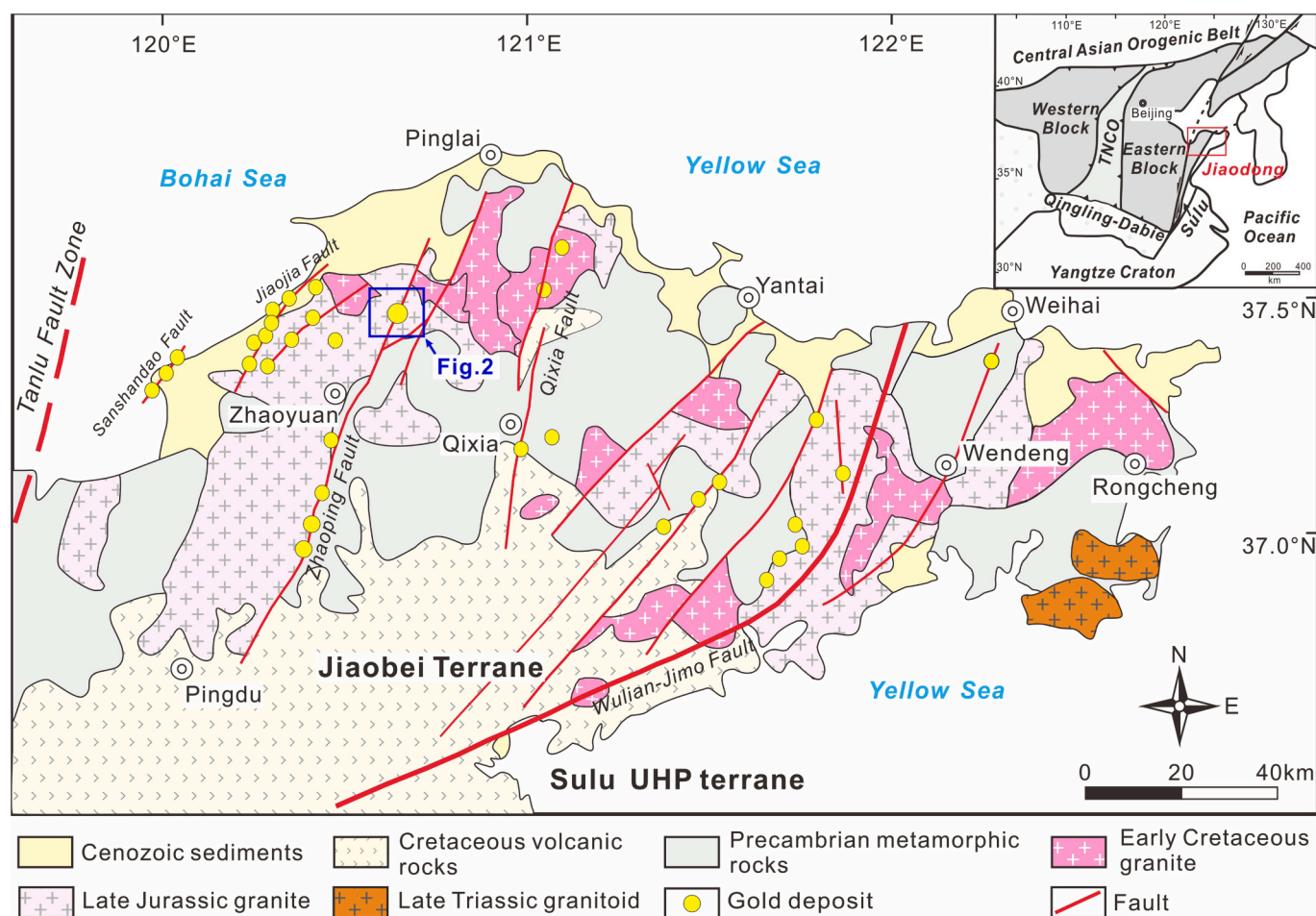

Fig. 1. Simplified geologic map of the Jiaodong Peninsula showing the Precambrian basement rocks, Mesozoic igneous rocks, and major gold deposits (after Deng et al., 2020b). Inset shows tectonic blocks of the NCC and location of the Jiaodong Peninsula (after Zhao et al., 2005). Abbreviations: TNCO = Trans-North China Orogen; UHP = ultrahigh-pressure. (For interpretation of the references to colour in this figure legend, the reader is referred to the web version of this article.)

NE-striking brittle-ductile faults, which underwent multiple reactivations during the late Mesozoic (Deng et al., 2015). These faults played a significant role in controlling the distribution and localization of gold deposits in the region (Fig. 1).

The Jiaodong Peninsula hosts numerous world-class gold deposits that altogether contain a gold reserve of >5000 t and arguably form the third largest gold province in the world (Song et al., 2022). These gold deposits are predominantly hosted in the Late Jurassic to Early Cretaceous granitic intrusions and, to a lesser extent, in the Precambrian metamorphic rocks (Li et al., 2006; Deng et al., 2020b; Zhang et al., 2020; Fan et al., 2021). Mafic dikes are well-developed in the mining areas and are generally parallel to, intruding, and/or cross-cut by gold lodes (e.g., Fig. 2; Tan et al., 2012; Zhu et al., 2020). Based on the style of mineralization, the gold deposits in the Jiaodong Peninsula are broadly classified into quartz-sulfide vein type and disseminated/stockwork type. However, these two mineralization styles can coexist within the same deposit as observed in the Linglong gold deposit, where quartz-sulfide veins occur predominantly in the shallower parts and disseminated/stockwork orebodies occur in the deeper parts (Song et al., 2022). Hydrothermal alteration is well-developed in these gold deposits and is characterized by sericite-quartz-pyrite (SQP) alteration within and around the gold lodes that are enveloped by a K-feldspar alteration zone. Geochronological studies using pyrite Rb—Sr, sericite ^{40}Ar—^{39}Ar, and monazite U—Pb dating have revealed that gold deposits in the Jiaodong gold province mostly formed in a short interval at 120 ± 2 Ma (Yang and Zhou, 2001; Li et al., 2003, 2006; Deng et al., 2020b; Feng et al., 2020; Zhang et al., 2020; Li et al., 2022). This period coincided with intensive thinning of the lithospheric mantle and upwelling of the asthenosphere beneath the eastern NCC (Zhu et al., 2011).

The Linglong gold deposit is situated in the northern extent of the Zhaoping Fault (Fig. 1). The gold lodes in this deposit are predominantly hosted in the Late Jurassic Linglong granite and structurally controlled by the Potouqing, Linglong, and Jiuqujiangjia faults (Fig. 2). The deposit was dominated by quartz-sulfide vein type mineralization with an estimated gold reserve of ca. 400 t (Song et al., 2022). However, during exploration and mining, more prominent disseminated/stockwork orebodies have been discovered at depth, which reveal a gold reserve of nearly twice of the quartz-sulfide veins (Song et al., 2022). In view of field relationships and mineral assemblages, four paragenetic stages are identified. Pre-mineralization stage I is featured by abundant K-feldspar associated with milky quartz and minor pyrite. Stage II is largely represented by quartz-pyrite veins/veinlets and/or disseminations overprinting the mineral assemblages of stage I. Stage III consists of quartz-pyrite veins containing variable amounts of galena, chalcopyrite, and sphalerite. Gold mineralization mainly occurs in stages II and III, as native gold intergrown with pyrite, chalcopyrite, galena, and sphalerite (Lin et al., 2019; Xiong et al., 2021; Li et al., 2022; Li et al., 2023). Sericite is also well-developed in these two stages and is intimately associated with the gold-bearing sulfides. Stage IV is marked by the assemblage of quartz-calcite typically without gold mineralization. In summary, stage I is characterized by K-feldspar alteration, whereas SQP alteration characterizes stages II and III. Carbonation mainly occurs in the final mineralization stage.

3. Samples and analytical methods

Eight samples were selected from underground tunnel of the Linglong gold deposit for trace element and Li isotopic analyses. They are strategically distributed along a cross section from the unaltered Linglong granite ($n = 1$), through variably K-feldspar-altered granites ($n = 3$), to disseminated gold orebodies associated with SQP alteration ($n = 4$; Fig. 3). The unaltered Guojialing granite ($n = 2$) and its mafic enclaves ($n = 2$), Early Cretaceous basalts ($n = 2$; Pei et al., 2004), mafic dikes either cutting ($n = 1$) or intersected by ($n = 2$) gold lodes, and metamorphic rocks of the Jiaodong Group ($n = 1$) were also sampled and analyzed for comparison. Separately, 12 samples with typical mineral assemblages of stages I to III were collected for in-situ oxygen isotopic analysis and microthermometry. All samples were firstly prepared as standard thickness (doubly) polished thin sections and examined using optical microscopy. Further examination was conducted utilizing a scanning electron microscope (SEM) equipped with an energy-dispersive spectrometer (EDS). To gain deeper insights into mineral
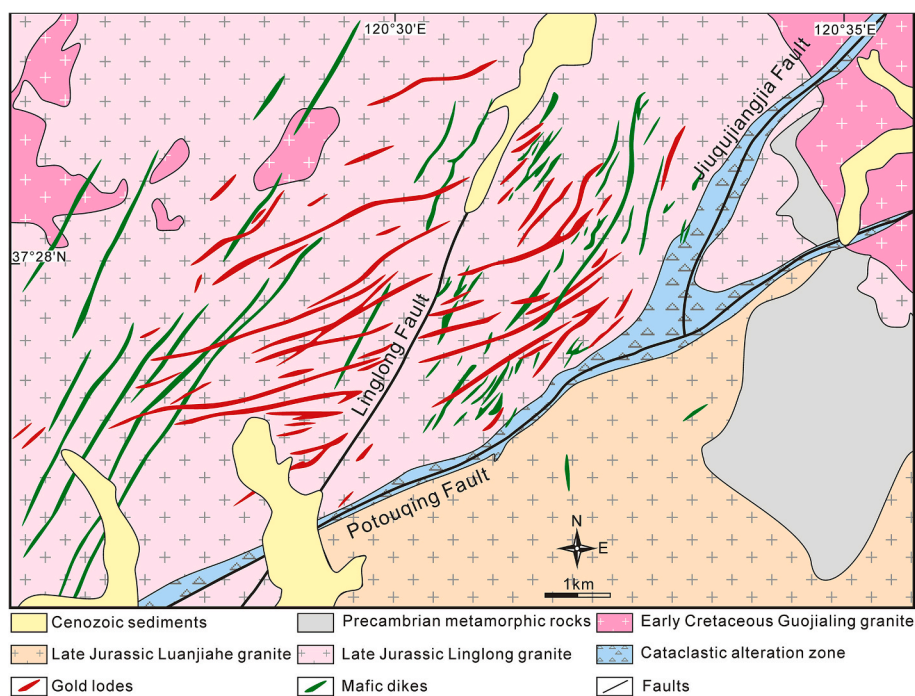

Fig. 2. Geologic map of the Linglong gold deposit showing that gold lodes are hosted in the Linglong granite and strictly controlled by the NE-trending structures (after Li et al., 2022). Mafic dikes are widespread in the gold mine, which cross-cut and/or are intercepted by gold lodes. (For interpretation of the references to colour in this figure legend, the reader is referred to the web version of this article.)
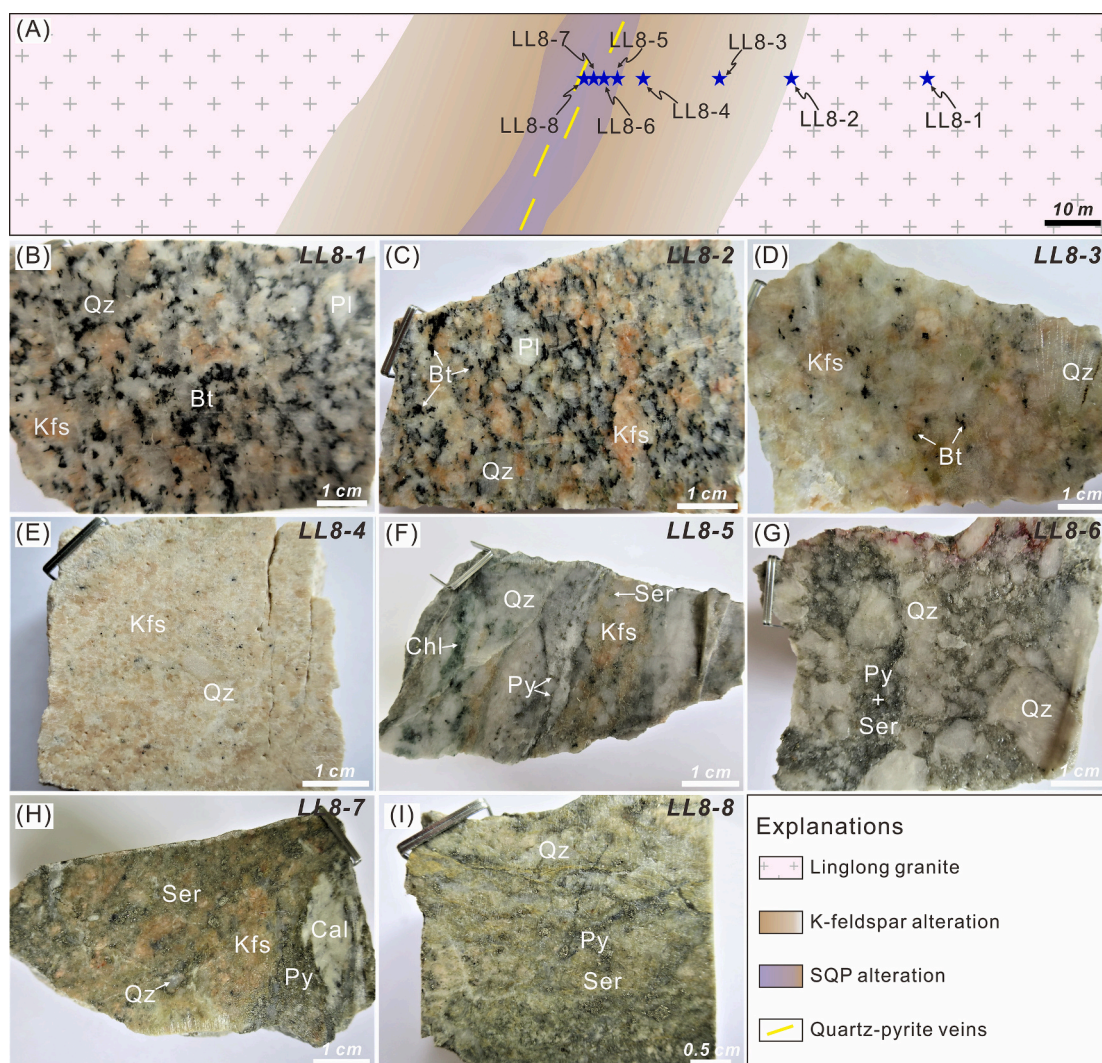
Fig. 3. Sketch (A) and photographs (B—I) illustrating the geometry and alteration zones of a typical gold lode at the Linglong deposit. The gold lode is characterized by SQP alteration, of which bound by the K-feldspar alteration zone and further outwards by hosting unaltered Linglong granite at both sides. The blue stars in Fig. 3A only indicate the approximate locations of the 8 samples relative to different alteration zones. Abbreviations: Qz = quartz; Pl = plagioclase; Kfs = K-feldspar; Bt = biotite; Py = pyrite; Ser = sericite; Chl = chlorite; Cal = calcite. (For interpretation of the references to colour in this figure legend, the reader is referred to the web version of this article.)

assemblages, paragenesis, and textures, a JXA-8230 electron probe microanalyzer equipped with a MonoCL detector was employed. Areas of interest for quartz in-situ oxygen isotopic analysis were drilled out from the thin sections and mounted at the center (5 mm in diameter) of the epoxy disks of 25 mm in diameter along with the analytical standards, zircon Qinghu (Li et al., 2013) and quartz NBS-28 (Coplen et al., 1983).

3.1. Whole-rock trace element analysis

Trace element compositions of unaltered and variably altered granites, mafic enclaves, basalts, mafic dikes, and metamorphic rocks were analyzed using inductively coupled plasma mass spectrometry (ICP-MS) at the State Key Laboratory of Ore Deposit Geochemistry (SKLODG), Institute of Geochemistry, Chinese Academy of Sciences (IGCAS). The analytical procedures are the same as those presented by Qi and Grégoire (2000) and are briefly described here. Rock powders of ca. 50 mg were put into Teflon bombs and dissolved by concentrated HF-HNO$_3$ (3:1) at 180 °C for 2 days. Then the solutions were dried and re-dissolved in HNO$_3$ at 180 °C for 1 day, which were measured by ICP-MS. Rhodium (1 ml of 1 μg/ml; Qi and Grégoire, 2000) and two USGS standards

(BHVO-2 and W-2; Fourny et al., 2016) were used as internal standard and unknown to control signal drift of the instrument and monitor the data quality, respectively. The precision assessed by replicate analyses of BHVO-2 and W-2 was better than 5% for all reported elements. The accuracy estimated by the two external standards was within 6% of the recommended values for all reported elements.

3.2. Lithium isotopic analysis

The Li isotopic compositions were analyzed at SKLODG in IGCAS. Details for the analysis can be found in Xu et al. (2019) and are briefly summarized here. Rock powders were digested by a mixture of HNO$_3$ and HF at 180 °C for 2 h. After several evaporation and redissolution by HNO$_3$ and HCl, the solutions were purified through a two-step column chemistry to isolate Li from the sample matrix. The final solutions were dried and redissolved in 2% v/v HNO$_3$ for isotopic analysis using a Neptune MC-ICP-MS. The two Li isotopic ions ^{7}Li$^+$ and ^{6}Li$^+$ were collected in a high-mass Faraday cup (H4) and a low-mass cup (L4), respectively. Lithium isotope standard solution (IRMM-016; Millot et al., 2004), rock reference (BCR-2; Penniston-Dorland et al., 2012), and seawater (CASS-5; Xu et al., 2019) were treated as unknown to monitor

the isotopic fractionation during the chemical pre-treatment. All data was reported in δ^7Li relative to IRMM-016. Individual samples investigated in this study were analyzed in duplicate separately.

3.3. In-situ oxygen isotopic analysis

In-situ oxygen isotopic analysis of quartz was conducted using a CAMECA IMS 1280-HR secondary ion mass spectrometer at the Guangzhou Institute of Geochemistry, Chinese Academy of Sciences. Details for the analysis are given in Yang et al. (2018) and briefly given here. Ions of Cs^+ were used as the primary ion beam with an intensity of ~2 nA and accelerating voltage of 10 kV. The analytical spots exhibit an elliptical shape with the length, width, and depth of ~20, 10, and 1 μm, respectively. The oxygen isotopes ^{18}O and ^{16}O were measured using the multi-collection mode on two off-axis Faraday cups, yielding the ^{16}O intensity typically of ~2×10^9 cps. Zircon standard Qinghu ($\delta^{18}O$ = 5.46 ‰; Li et al., 2013) and quartz standard NBS-28 ($\delta^{18}O$ = 9.64 ‰; Coplen et al., 1983) were used to correct the instrumental mass fractionation and monitor the data quality, respectively. The obtained $^{18}O/^{16}O$ values were normalized to Vienna Standard Mean Ocean Water (V-SMOW; $^{18}O/^{16}O$ = 0.0020052; Baertschi, 1976) and expressed with the $\delta^{18}O$ notation.

3.4. Fluid inclusion microthermometry

Fluid inclusion petrography was firstly conducted to identify the phase, occurrence, and association of fluid inclusions, with the application of fluid inclusion assemblage (FIA) concept (Goldstein and Reynolds, 1994). Selected fluid inclusions were then analyzed for microthermometry using a Linkham THMS-600 heating-freezing stage equipped with an Olympus BX51 microscope at the State Key Laboratory of Geological Processes and Mineral Resources, China University of Geosciences, Wuhan, China. Uncertainties of the measurements are ±2 °C for runs in the range of 100° to 600 °C. As the fluid inclusion microthermometry in this study is utilized to calculate $\delta^{18}O$ values of hydrothermal fluid equilibrated with quartz, thus only total homogenization temperature (T_h) was measured.

4. Results

4.1. Bulk rock trace element compositions

The trace element compositions of various rocks are presented in Supplementary Table A1. Eight samples progressively altered from unaltered granite (LL8–1), through increasingly K-feldspar-altered granites (LL8–2 to LL8–4), to increasingly SQP-altered granites (LL8–5 to LL8–8) (Fig. 3) are shown in Fig. 4. The trace element variations in rocks with increasing alteration can be summarized into three distinct trends (Fig. 4). The first trend is typically featured by an increase in Ba and Sr concentrations with increasing K-feldspar alteration, followed by a sharp decrease when K-feldspar is further altered to the SQP assemblage (Fig. 4A, B). In contrast, Li, Th, U, and REE show gradual depletion
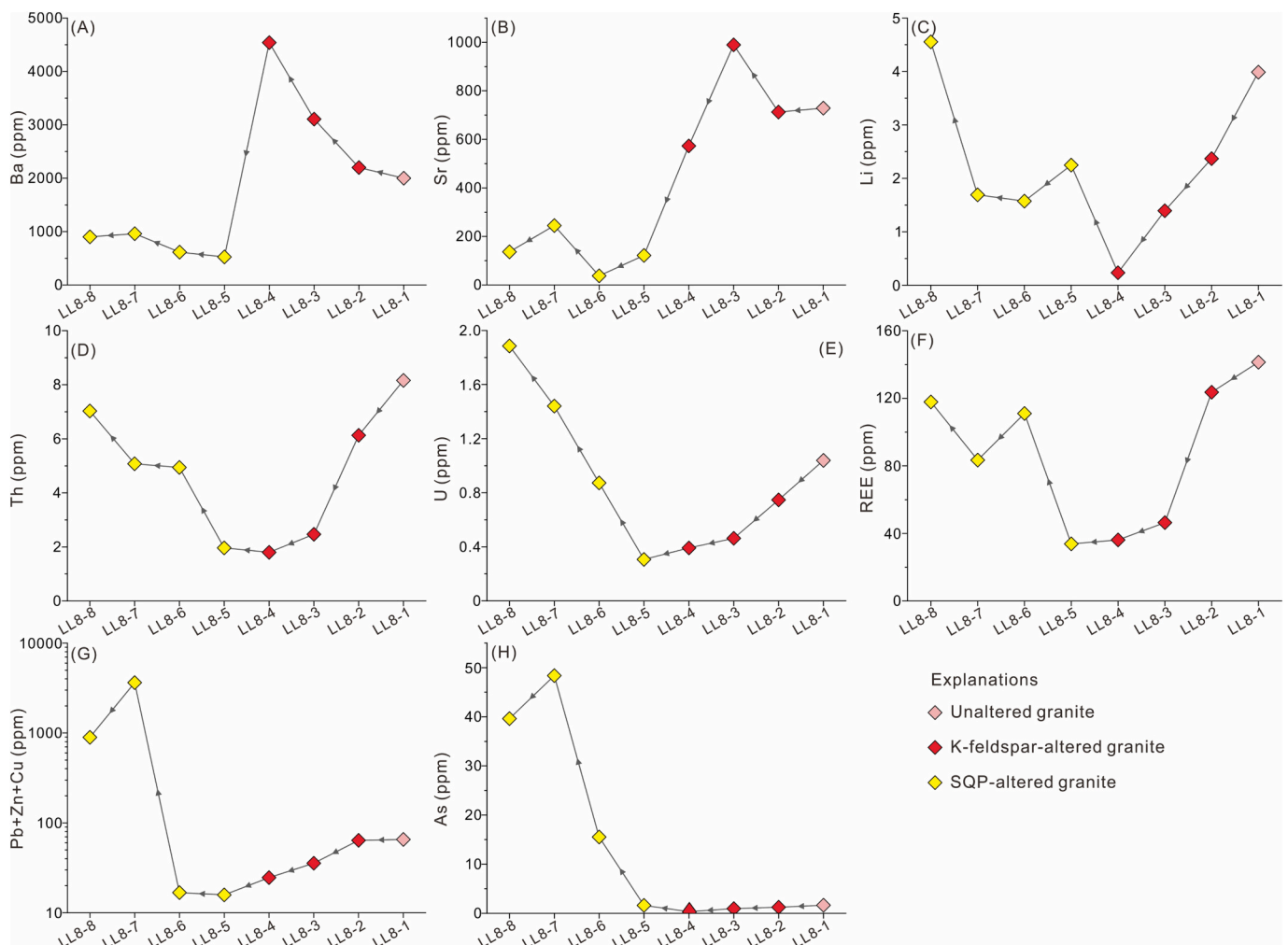

Fig. 4. Variations of Ba (A), Sr (B), Li (C), Th (D), U (E), REE (F), Pb + Zn + Cu (G), and As (H) contents for samples from this study. For more details see the text.

during the progressive K-feldspar alteration, but their contents subsequently increase with intensifying SQP alteration (Fig. 4C-F). The third trend is characterized by elements generally having positive correlations with Au at the Linglong gold deposit, namely Pb, Zn, Cu, and As (Lin et al., 2019; Li et al., 2022). These elements show a slight decrease or remain relatively constant during increasing K-feldspar alteration, but their contents gradually increase due to progressive SQP alteration (Fig. 4G, H).

4.2. Lithium isotopic compositions

Whole rock Li isotopes are presented in Supplementary Table A2 and illustrated in Fig. 5. Metamorphic rocks of the Jiaodong Group yield $\delta^7 Li$ values of $-1.48 \sim -1.26$ ‰. Early Cretaceous basalts and mafic dikes have $\delta^7 Li$ values of 3.98–5.69 ‰ and 2.46–5.65 ‰, respectively. Such isotopic compositions are consistent with those of mantle rocks (1.5–5.6 ‰; Tomascak, 2004; Marschall et al., 2017). The $\delta^7 Li$ values of the Guojialing granites and the enclosed mafic enclaves are 4.03–4.90 ‰ and 3.16–6.69 ‰, respectively. Although statistically comparable to mantle values, these $\delta^7 Li$ values are also consistent with those commonly observed in granites worldwide (e.g., Bryant et al., 2004; Tomascak, 2004; Magna et al., 2010). The unaltered Linglong granite has the highest $\delta^7 Li$ values of 11.69–11.72 ‰ (mean = 11.71 ‰). Along the studied cross section, the $\delta^7 Li$ values exhibit a gradual decrease from 11.72 ‰ in the unaltered granite to -8.00 ‰ in the strongly K-feldspar-altered granite (Fig. 5). However, the $\delta^7 Li$ values of the altered granites increase towards the central mineralization zone where K-feldspar was altered to SQP (Fig. 5). Both Li concentrations and $\delta^7 Li$ values are positively correlated for the 8 samples along the cross section but unique trends are defined for the K-feldspar and SQP alterations, respectively (Fig. 5).

4.3. Quartz microtextures, fluid inclusion petrology, and microthermometric result

Quartz from the pre- (stage I) and syn- (stages II and III) mineralization stages can be well distinguished by their cathodoluminescence (CL) images (Fig. 6). The milky quartz of stage I shows homogeneous to patchy textures under CL images, which are commonly fractured and subsequently infilled by later stage quartz (Fig. 6A-D). Gray quartz of stage II is relatively darker compared to that of stage I and exhibits mottled to homogeneous textures in CL images (Fig. 6B-D). This generation of quartz is typically intergrown with pyrite and sericite, and it intrudes or overgrows the stage I quartz (Fig. 6B-D). Quartz of stage III mostly occurs as fine-grained euhedral crystals and is intimately associated with sphalerite, chalcopyrite, and other sulfides (Fig. 6E, F). The quartz grains display brighter, patchy cores and darker, oscillatory rims (Fig. 6E, F).

Three types of fluid inclusions were identified by microscopic observation at room temperature ($\sim 30\,°C$), including abundant biphase and less amounts of triphase H_2O-CO_2-$NaCl$ inclusions (Fig. 7). The biphase fluid inclusions contain an aqueous phase and one CO_2 phase (Fig. 7A-D). The CO_2 phase is either CO_2 vapor or CO_2 liquid as demonstrated by previous Laser Raman studies (e.g., Yang et al., 2016; Guo et al., 2020). This type of fluid inclusion can be further divided into H_2O-rich H_2O-CO_2-$NaCl$ inclusions and CO_2-rich H_2O-CO_2-$NaCl$ inclusions, with the volume of the carbonic phase being of 10–50% and 60–90%, respectively (Fig. 7A-D). The H_2O-rich H_2O-CO_2-$NaCl$ inclusions comprise >80% of the biphase fluid inclusions. The carbonic phases in the triphase H_2O-CO_2-$NaCl$ inclusions generally account for 10–50% of the total volume (Fig. 7E-H). These three types of fluid inclusions are developed in quartz of all the three paragenetic stages. Fluid inclusions in the investigated samples occur in various modes, including along growth zones (Fig. 7A, B), in short trails within crystals (Fig. 7C) and long trails crosscutting crystal boundaries, in cluster (Fig. 7D-F), and as isolations (Fig. 7G, H). Fluid inclusions along growth zones and in isolations are likely primary, while those forming short intra-crystal
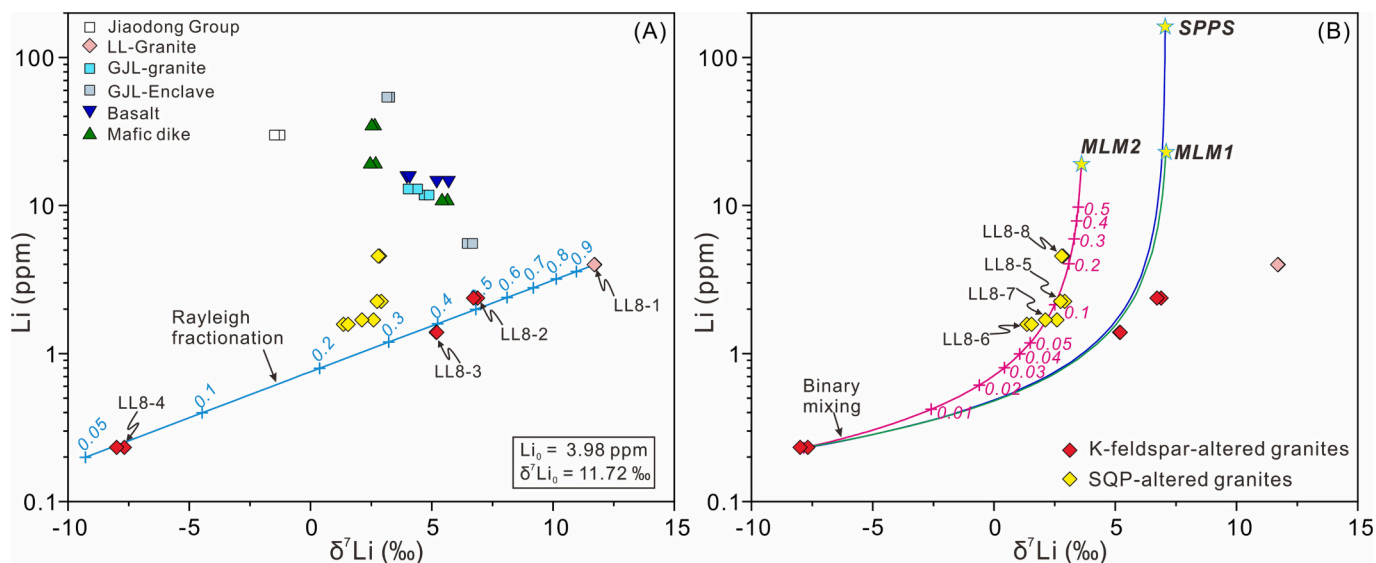

Fig. 5. Lithium isotopic composition versus Li concentration diagrams for samples from this study. The values of the Precambrian metamorphic rock of Jiaodong Group, Guojialing granites and the enclosed enclaves, and Early Cretaceous basalts and mafic dikes are also shown for comparison. The Rayleigh fractionation line in Fig. 5A was modeled by $\delta^7 Li_{altered\ rocks} = [\delta^7 Li_0 + 1000] \times f^{(\alpha-1)}-1000$, where $\delta^7 Li_0$ and $\delta^7 Li_{altered\ rocks}$ are the Li isotopic compositions of the unaltered and altered granite. The factor f is the fraction of Li remaining in the rocks ($f = Li_{altered\ rocks}/Li_0$), where Li_0 and $Li_{altered\ rocks}$ are the respective Li concentrations of the unaltered and altered granite. The factor α is Li isotopic fractionation factor (1.007; Chan et al., 1993). The binary mixing lines in Fig. 5B were modeled by $Li_{altered\ rocks} = Li_A \times f + Li_B \times (1-f)$ and $\delta^7 Li_{altered\ rocks} = [\delta^7 Li_A \times Li_A \times f + \delta^7 Li_B \times Li_B \times (1-f)]/Li_{altered\ rocks}$, where $Li_{altered\ rocks}$, Li_A, and Li_B are the Li concentrations of altered granite, and endmembers A and B, respectively, and $\delta^7 Li_{altered\ rocks}$, $\delta^7 Li_A$, and $\delta^7 Li_B$ are the corresponding $\delta^7 Li$ values, respectively. The value f is the contribution fraction of end member A. The term SPPS refers to fluids from devolatilization of subducted paleo-Pacific plate and the overlying sediments. The term MLM1 refers to fluids from devolatilization of metasomatized lithospheric mantle whereas MLM2 refers to fluids from degassing of metasomatized lithospheric mantle-derived mafic magma.
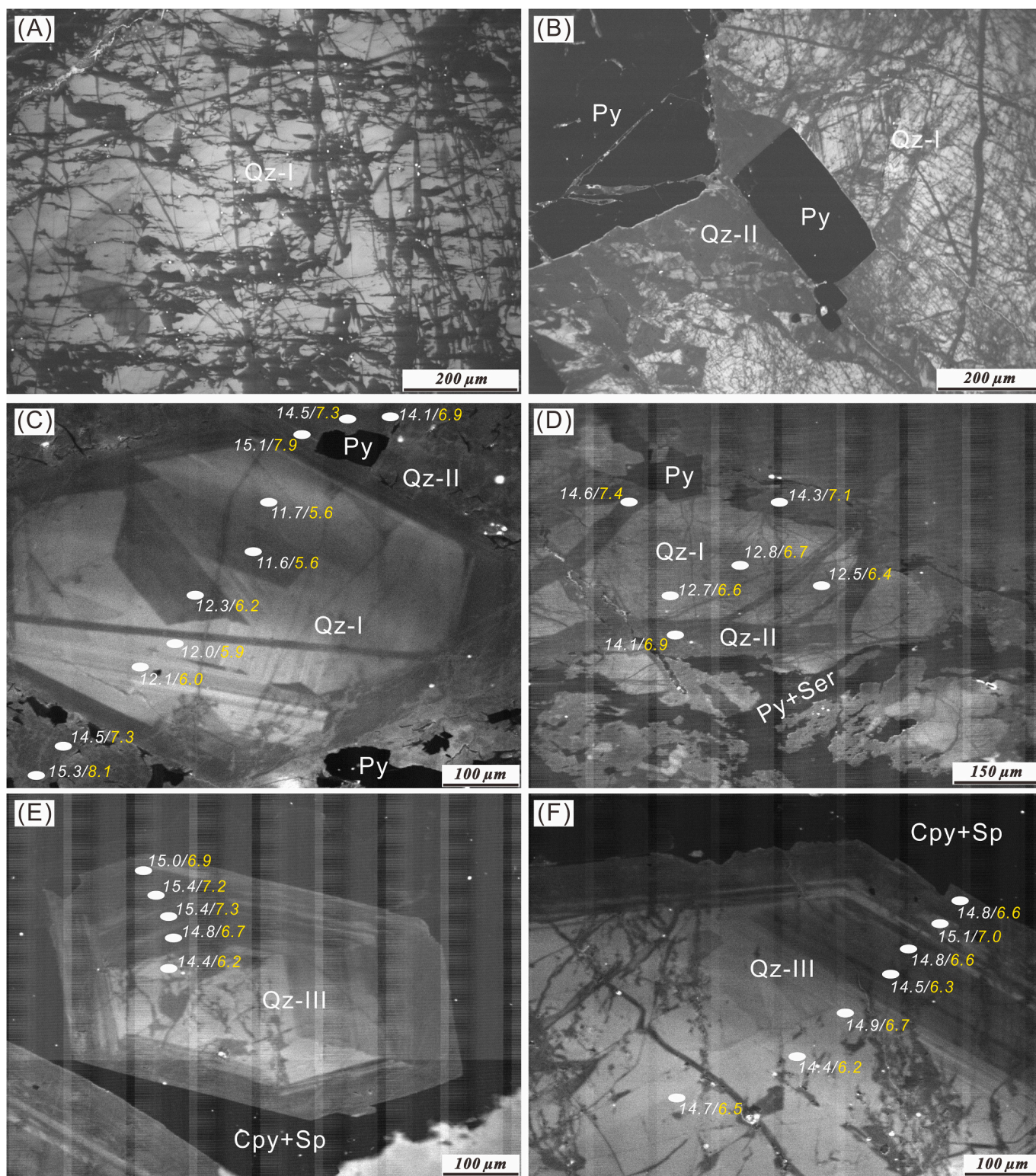
Fig. 6. Representative SEM-CL images showing microtextures of stages I-III quartz at the Linglong lode gold deposit. The ellipse dots indicate the locations of SIMS oxygen isotopic analysis, and the adjacent numbers are measured $\delta^{18}O_Q$ (white) and calculated $\delta^{18}O_W$ (yellow) values using the mean fluid inclusion homogenization temperatures. A. Stage I quartz exhibiting homogeneous to patchy textures. B. Brighter quartz of stage I was crosscut by darker quartz of stage II that is intergrown with pyrite. C. Compositional quartz consisting of brighter, patchy core of stage I quartz and darker, mottled rim of stage II quartz. The quartz rim is intergrown with numerous fine-grained pyrite. D. Stage II mineral assemblage of sericite-quartz-pyrite crosscutting stage I quartz. E, F. Fine-grained stage III quartz are intergrown with chalcopyrite and sphalerite. The quartz grains show patchy core and oscillatory-zoned rim. Abbreviations: Qz = quartz; Py = pyrite; Ser = sericite; Cpy = chalcopyrite; Sp = sphalerite. (For interpretation of the references to colour in this figure legend, the reader is referred to the web version of this article.)
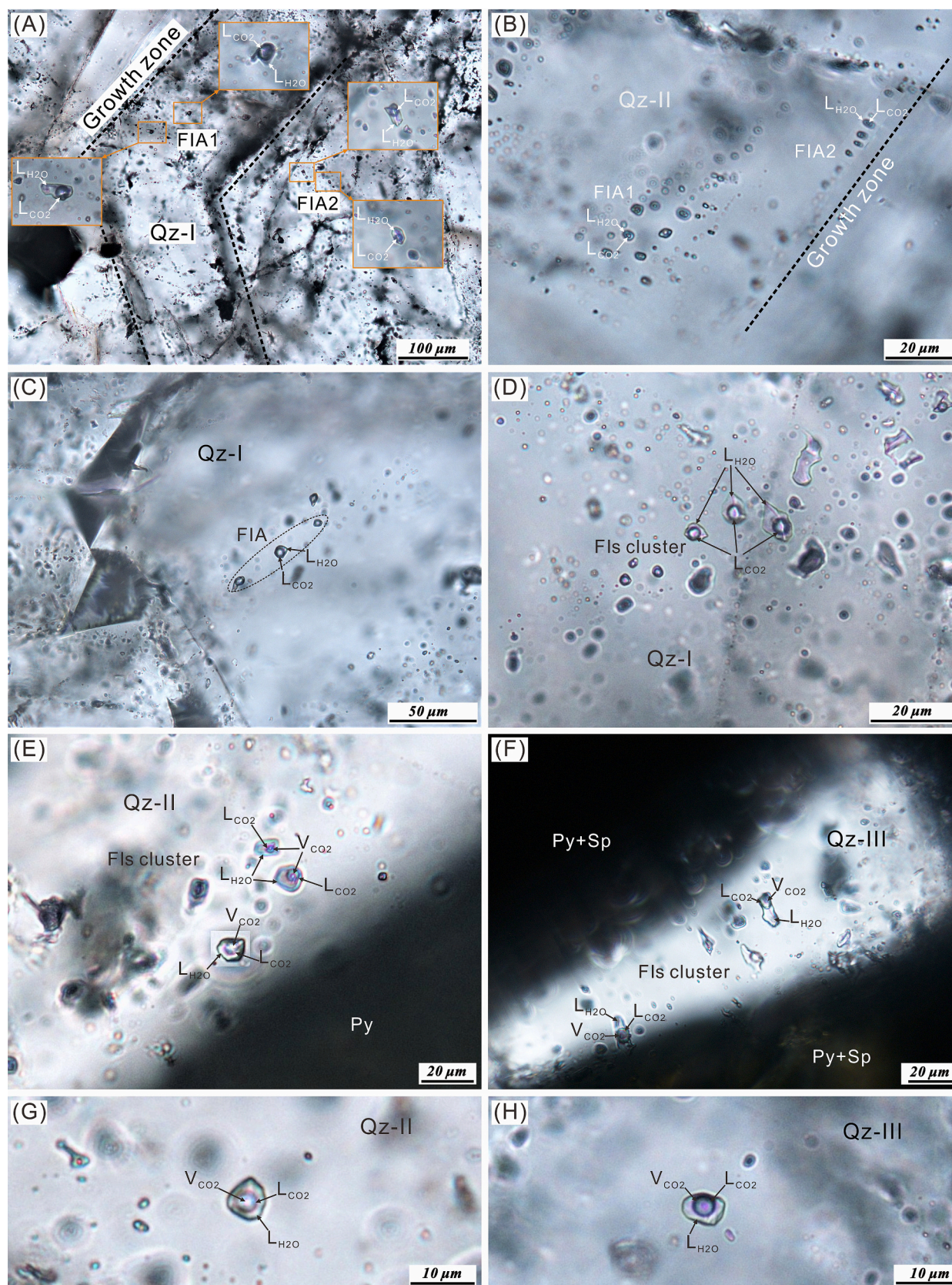
Fig. 7. Photomicrographs showing types and occurrences of fluid inclusions trapped in quartz of the three paragenetic stages. A, B. Biphase fluid inclusions along growth zones of stages I and II quartz and respectively forming two FIAs. C. Biphase fluid inclusions forming a short intra-crystal trail and a FIA. D. Biphase fluid inclusions in a cluster. E. Triphase fluid inclusions in a cluster that are adjacent to pyrite. F. Triphase fluid inclusion cluster in a quartz grain enclosed by pyrite and sphalerite. G, H. Isolated triphase fluid inclusion in stages II and III quartz, respectively. Abbreviations: Qz = quartz; Py = pyrite; Sp = sphalerite.

trails and clusters are likely pseudosecondary (Roedder, 1984; Chi and Lu, 2008; Chi et al., 2021). Fluid inclusions in inter-crystal trails are secondary. According to the definition of Goldstein and Reynolds (1994), fluid inclusions along growth zones and short intra-crystal trails form FIAs, the T_h of which can more reliably be utilized to calculate oxygen isotope fractionation between quartz and the equilibrated hydrothermal fluid. As such, only FIAs were measured in this study.

The microthermometric data are listed in Supplementary Table A3. The data for individual FIAs are grouped together. The individual FIAs investigated in this study have T_h value variation <15 °C, which are considered to be a criterion for "good FIA" (e.g., Goldstein and Reynolds, 1994). The FIAs in stage I quartz have T_h values of 312° to 349°C, with mean value of 330 °C. These values for FIAs in quartz of stage II are 272°-318 °C and 295 °C, respectively. The FIAs in quartz of stage III have T_h values of 246° to 307 °C, yielding mean value of 270 °C.

4.4. Quartz oxygen isotopes

The $\delta^{18}O$ values for quartz and the equilibrated fluid from stages I to III are presented in Supplementary Table A4 and graphically shown in Figs. 6 and 8. Stage I quartz is characterized by variable oxygen isotopes, yielding $\delta^{18}O_Q$ values in a range of 10.9–14.7 ‰ (mean = 12.9 ‰, s.d. = 1.0; Figs. 6, 8). Based on microthermometric data of fluid inclusions in stage I quartz and the quartz-water fractionation equation (Sharp et al., 2016), the $\delta^{18}O_W$ values of hydrothermal fluid equilibrated with stage I quartz are 4.3–9.2 ‰ (Fig. 8). Quartz of paragenetic stage II has higher $\delta^{18}O_Q$ values of 13.7–15.3 ‰ (14.5, 0.4), corresponding to $\delta^{18}O_W$ values of the equilibrated hydrothermal fluid of 5.6–8.9 ‰ (Fig. 8). Stage III quartz exhibits the highest $\delta^{18}O_Q$ values ranging from 14.4 to 15.6 ‰ (14.9, 0.4). The $\delta^{18}O_W$ values of the equilibrated hydrothermal fluid are 5.2–8.8 ‰ (Fig. 8).

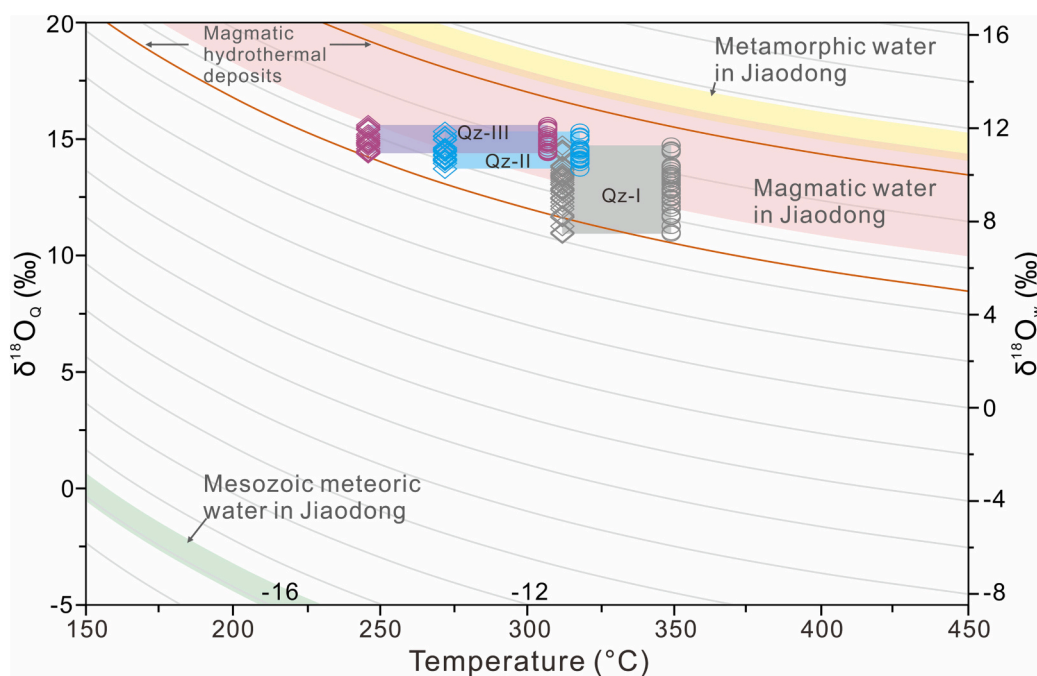## 5. Discussion

5.1. Elemental behaviors during hydrothermal alteration

A systematic change in mineral assemblages is observed from the unaltered granite to K-feldspar- and SQP-altered granites (Fig. 3), which likely controls the variations of trace element concentrations along the cross section. Previous studies have shown that hydrothermal K-feldspar contains higher Ba and Sr contents than magmatic K-feldspar in the Linglong granite (e.g., Zhang et al., 2017; Wang, 2021). Consequently, the increase in Ba and Sr concentrations from samples LL8–1 to LL8–4 can be attributed to the formation of abundant hydrothermal K-feldspar during the K-feldspar alteration. Conversely, the sharp decrease in Ba and Sr concentrations in SQP-altered granites is a result of alteration of K-feldspar to sericite and quartz, leading to the loss of these mobile elements to the fluids. The variations of Li content are controlled by decomposition of biotite during the K-feldspar alteration and formation of sericite during the SQP alteration because mica preferentially uptakes Li compared to feldspar, quartz, and pyrite (Bea et al., 1994; Icenhower and London, 1995; Li et al., 2018a; Bao et al., 2021). The variations of Th, U, and REE contents are generally associated with the dissolution of magmatic accessory minerals (e.g., titanite, monazite) during the K-feldspar alteration, followed by the re-precipitation of hydrothermal titanite and monazite during the subsequent SQP alteration (e.g., Deng et al., 2020b; Li et al., 2022). The dissolution of minor magmatic sulfides in the granite during the K-feldspar alteration likely accounts for the gradual decrease of ore-related Pb, Zn, Cu, and As concentrations. Whereas deposition of ore sulfides associated with intensifying SQP alteration is responsible for the rising concentrations of these elements. These variations in minerals and elements suggest that the SQP alteration, rather than the K-feldspar alteration, is spatially associated with the gold mineralization (Fig. 3).

Fig. 8. Plot showing $\delta^{18}O$ values of quartz and fluids equilibrated with quartz of the three paragenetic stages at the Linglong lode gold deposit. The temperatures used here are the lowest (diamonds) and highest (circles) values of fluid inclusion homogenization temperature ranges affiliated with individual stages. The gray, light-blue, and purple boxes are the respective $\delta^{18}O_Q$ and $\delta^{18}O_W$ ranges of stages I, II, and III. Isopleths of $\delta^{18}O$ values are calculated using the quartz-water $\delta^{18}O$ fractionation equation of Sharp et al. (2016). The $\delta^{18}O$ ranges of magmatic and metamorphic waters in Jiaodong are calculated from the $\delta^{18}O$ values of magmatic biotite and K-feldspar in various late Mesozoic granitoids and metamorphic mica in basements (Mao et al., 2005). The $\delta^{18}O$ fractionation equations for mica and K-feldspar were from Zheng (1993) and Bottinga and Javoy (1973), respectively, where the temperatures were 620 °C for magmatic biotite (Sai et al., 2016; Yang et al., 2017), 550 °C for magmatic K-feldspar (Sai et al., 2016; Yang et al., 2017), and 500 °C for metamorphic mica (Tomkins, 2010). The $\delta^{18}O$ range of Mesozoic meteoric water in Jiaodong is from Zhang et al. (1995). The $\delta^{18}O$ range of fluids responsible for magmatic-hydrothermal deposits (5–10 ‰) is from Taylor (1974). (For interpretation of the references to colour in this figure legend, the reader is referred to the web version of this article.)

5.2. Lithium isotope fractionation during hydrothermal alteration

Lithium is a mobile alkaline element with two isotopes [6]Li and [7]Li fractionating readily during fluid-rock interactions (Penniston-Dorland et al., 2017). As such, lithium isotopes are a powerful tool in studying hydrothermal alteration, identifying fluid sources, and tracing fluid evolutions (e.g., Bernal et al., 2014; Nadeau et al., 2021; Xu et al., 2021). The behavior of Li during fluid-rock interaction is predominantly governed by temperature. At lower temperatures (<150 °C; e.g., seawater-rock interaction), lithium is removed from the fluid and incorporated into alteration phases (Chan et al., 1992). Conversely, at higher temperatures (>200 °C), lithium is leached from the hosting rocks into the fluid (Wunder et al., 2007). As [7]Li partitions preferentially into the coexisting fluid while [6]Li becomes enriched in minerals like micas, the effect of such leaching would impart a lighter δ^7Li signature in the altered rocks and hence a heavier δ^7Li signature in the fluids (Penniston-Dorland et al., 2017). The magnitude of Li isotope fractionation in these processes is also affected by temperature (Chan et al., 1992; Wunder et al., 2006). In cases where the concentrations of Li remaining in the altered rocks are very low, their original Li isotopic compositions would have mostly been erased by the alteration. Further interaction with a fluid with contrast Li contents and δ^7Li values would then impart the Li elemental and isotopic characteristics of the fluid onto the altered rocks (i.e., fluid buffering; Brant et al., 2012; Liu et al., 2022). Therefore, a combination of Li concentrations and δ^7Li values could be used to determine the source of the equilibrated fluid.

The unaltered Linglong granite has δ^7Li values up to 11.72 ‰, which is considerably higher than the values typically observed in most granites worldwide (−5 to 8 ‰; e.g., Bryant et al., 2004; Tomascak, 2004; Magna et al., 2010). However, similarly high values have been reported for granites in other regions such as the Canadian Shield (11.3 ‰; Bottomley et al., 2003), Saxo-Thuringian Zone in Germany (14.7 ‰; Romer et al., 2014), and Tibet in China (10.3 ‰; Lu et al., 2021). The origin of these high δ^7Li granites is commonly attributed to derivation from [7]Li-rich reservoirs (e.g., Chan et al., 2006; Tang et al., 2007; Lu et al., 2021) or interactions with [7]Li-rich rocks/fluids (e.g., Romer et al., 2022).

The transition from the unaltered to intensively K-feldspar-altered granites is accompanied by a decreasing trend in both Li concentrations and δ^7Li values (Fig. 5A). This trend can potentially be explained by mixing of different reservoirs or Rayleigh fractionation (e.g., Rudnick et al., 2004; Teng et al., 2006; Bao et al., 2021; Liu et al., 2022). The first possibility can be precluded in this study as no reservoirs with extremely low δ^7Li values and Li concentrations for the fluid were observed in the Jiaodong gold province (Fig. 5). In view of fluid inclusion data that stage I quartz has homogenization temperatures higher than 300 °C (349°-312 °C), we propose that the decreasing Li concentrations and δ^7Li values during the K-feldspar alteration was mostly governed by Rayleigh fractionation, during which Li was leached from the host granite into the hydrothermal fluid. This interpretation is further confirmed by samples from the unaltered to increasingly K-feldspar-altered Linglong granites are well plotted along the Rayleigh fractionation line (Fig. 5A).

When the K-feldspar-altered granites undergo further alteration to form the SQP alteration zones, and possibly the gold ores, their Li contents and Li isotopic compositions exhibit a covariant increase along a trend of steeper gradient (Fig. 5B). Such Li elemental and isotopic compositions cannot be explained by ongoing Rayleigh fractionation after the K-feldspar alteration, as it would result in much lower Li concentrations and δ^7Li values (e.g., Fig. 5A). Therefore, it is likely that a distinct process controlled the variations in Li elements and isotopes during the SQP alteration (e.g., Bao et al., 2021; Wang, 2021). In view that the K-feldspar alteration has induced the granites progressively depleted in Li towards the gold lodes, it is expected that the intensively K-feldspar-altered granites, prior to their transformation into the SQP alteration zone, would contain very low Li concentrations (Fig. 5A). Therefore, the covariant increase in Li concentrations and δ^7Li values of the SQP-altered granites is likely caused by the buffering effect of the ore-fluid (e.g., Nishio et al., 2004; Teng et al., 2006; Tomascak et al., 2008; Brant et al., 2012; Bao et al., 2021; Liu et al., 2022).

5.3. Sources of ore-forming fluid

Quartz of the three paragenetic stages in the Linglong gold deposit were precipitated from a hydrothermal fluid in temperature ranges of 349°-312 °C, 318°-272 °C, and 307°-246 °C, with the respective means at ca. 330°, 295°, and 270 °C. Under such conditions, the oxygen diffusion in quartz can be neglected (Valley and Graham, 1991). Thus, the measured $\delta^{18}O_Q$ values can represent the original oxygen isotopes of quartz and the calculated $\delta^{18}O_w$ values can be reliably used to trace the source and evolution of the hydrothermal fluid. The calculated $\delta^{18}O_w$ values of the hydrothermal fluid equilibrated with stages I-III quartz range from 4.3 to 9.2 ‰ (Fig. 8), which are lower than the $\delta^{18}O_w$ values of metamorphic water in Jiaodong (10.6–11.8 ‰; Fig. 8) and ore-fluids typically related to Phanerozoic lode gold deposits formed by metamorphic devolatilization of sedimentary rocks (7–15 ‰; Goldfarb and Groves, 2015). However, these values are largely consistent with those of magmatic water in Jiaodong (6.5–10.9 ‰; Fig. 8) and magmatic-hydrothermal deposits worldwide (5–10 ‰; Fig. 8; Taylor, 1974). Therefore, a magmatic origin of the hydrothermal fluid is favored for the formation of the K-feldspar and SQP alteration zones in the Linglong gold deposit. The decreasing $\delta^{18}O_w$ values from stages I to III are likely caused by incursion of minor meteoric waters as suggested by previous studies (e.g., Wen et al., 2015).

The magmatic origin of the hydrothermal fluid is further supported by the Li isotopes. Three genetic models have been proposed for the source of ore-forming fluids in the Jiaodong Peninsula: (1) devolatilization of the subducted paleo-Pacific plate and the overlying sediments (e.g., Goldfarb et al., 2007; Groves et al., 2020); (2) direct devolatilization of metasomatized lithospheric mantle (e.g., Deng et al., 2020a); and (3) degassing of mafic magma derived from metasomatized lithospheric mantle (e.g., Li et al., 2012; Zhu et al., 2015; Wang et al., 2020). A binary mixing model using Li concentrations and δ^7Li values is adopted here to test the above hypotheses (Fig. 5B). In this model, the pre-ore Li-free K-feldspar-altered granite is considered to be "mixed" with fluids with different potential sources (e.g., Liu et al., 2022). The most intensively K-feldspar-altered granite sample LL8–4 is used as one endmember in this model, and further details regarding the model calculation can be found in the Supplementary material.

Assuming the subducted paleo-Pacific plate and the overlying sediments (Li: 23.8 ppm; δ^7Li: 3.58 ‰; Marschall et al., 2017) were the ultimate reservoirs, fluid through devolatilization of these rocks during greenschist- to amphibolite-facies metamorphism (ca. 2.9 wt% H_2O release; Goldfarb et al., 2005; Phillips and Powell, 2010; Tomkins, 2010; Wei and Zheng, 2020) would have a Li concentration of 164 ppm ($D_{Li}^{solid-fluid}$ = 0.12; Marschall et al., 2007) and a δ^7Li value of 7.06 ‰ ($\Delta^7Li_{fluid-rock}$, T = 500 °C; Wunder et al., 2006). Interaction and buffering of this fluid with the most intensively K-feldspar-altered granite cannot generate the Li concentrations and δ^7Li values of the SQP-altered granites observed in this study (Fig. 5B), which hence precludes the possibility of devolatilization of subducted paleo-Pacific plate and the overlying sediments as the dominant source of ore-forming fluid in the Linglong deposit.

Using the weighted average Li concentration and δ^7Li value of mafic dikes and basalts to represent partial melting products of the metasomatized lithospheric mantle beneath the NCC (Li: 19.0 ppm; δ^7Li: 3.61 ‰), the primitive Li concentration and δ^7Li value of the metasomatized lithospheric mantle would be 3.61 ppm ($D_{Li}^{solid-melt}$ = 0.10, 10% partial melting; Qiu et al., 2011; Ma et al., 2014) and 3.61 ‰ (as little Li isotopic fractionation takes place during partial melting; Tomascak et al., 1999; Schuessler et al., 2009; Li et al., 2018a), respectively. Fluid derived from the greenschist- to amphibolite-facies metamorphic devolatilization of the metasomatized lithospheric mantle (ca. 4.0 wt% H_2O release; Wei and Zheng, 2020) would have a Li concentration of 23.2 ppm and a δ^7Li

value of 7.09 ‰. Such fluid interaction and buffering with the most intensively K-feldspar-altered granite cannot produce the observed Li concentrations and δ^7Li values of the SQP-altered granites (Fig. 5B), implying that devolatilization of the metasomatized lithospheric mantle is not the predominant fluid source.

Similarly, we use the weighted average Li concentration and δ^7Li values of mafic dikes and basalts as the initial Li elemental and isotopic composition of mafic magma derived from the metasomatized lithospheric mantle. Fluid degassing from these magmas would have 19.3 ppm Li (2.0 wt% volatile degassing; $D_{Li}^{vapor-melt} = 0.30$; London et al., 1988) with broadly similar δ^7Li values, as little Li isotopic fractionation takes place during fluid exsolution (e.g., Li et al., 2018a). Interaction and buffering of this fluid with the intensively K-feldspar-altered granite align well with the observed Li concentrations and δ^7Li values of the SQP-altered granites (Fig. 5B). The model calculation implies a contributing proportion of mantle-derived magma at ca. 6–25% (Fig. 5B), consistent with previous estimations using noble gas isotopic compositions of the auriferous pyrite (Xue et al., 2013b; Wen et al., 2016; Tan et al., 2018; Liu et al., 2021). As such, we propose that Li, and by inference other volatiles and metals, responsible for gold mineralization in the Linglong gold deposit were mainly sourced from mafic magmas derived from the metasomatized lithospheric mantle.

5.4. A genetic model of the Linglong lode gold deposit

The above trace element and Li—O isotopic data suggest that magmatic fluids exsolved from the metasomatized lithospheric mantle-derived mafic magmas were responsible for the alteration and gold mineralization in the Linglong gold deposit. Integrating these findings with previous studies, a genetic model for the deposit can be proposed (Fig. 9). The subcontinental lithospheric mantle (SCLM) beneath the eastern NCC was intensively metasomatized by possible addition of minor gold and abundant volatiles prior to the late Mesozoic (e.g., Wu et al., 2019; Wang et al., 2020; Yang et al., 2021). The thinning of lithospheric mantle and upwelling of asthenosphere mantle during the Early Cretaceous induced partial melting of such fertile lithospheric mantle (Fig. 9). Mafic magmas derived from the metasomatized SCLM are denser than the continental crust, which were likely ponded at the transitional zones between the crust and mantle (Fig. 9; Herzberg et al., 1983; Muntean et al., 2011; Zhu et al., 2015). The extensional events during this period could have also formed and/or reactivated earlier-formed faults connecting to the lower crust (Zhu et al., 2010). Minor amounts of the mafic magma ascended rapidly along the extensional trans-lithospheric faults to form the basalts and mafic dikes (e.g., Zhang et al., 2002; Wang et al., 2022a). Meanwhile, significant amounts of the magma accumulated in the lower crust and then underwent considerable differentiation and fluid exsolution. Throughout these processes, gold was further enriched in the hydrothermal fluid by exsolution from the evolved mafic magma (Wang et al., 2020; Wang et al., 2022a; Li et al., 2023). The regional faults facilitated influx of auriferous hydrothermal fluid through the upper crust and the affiliated secondary and higher-order' faults provided loci for the ore-fluids accumulation (Li et al., 2012). The hydrothermal fluid metasomatized the Linglong granite and formed the wide-spread hydrothermal K-feldspar. In proximity to the fluid conduits, these granites underwent further alteration by the fluid, leading to the formation of the SQP alteration and associated gold mineralization (Fig. 9).

6. Conclusion

The giant Linglong gold deposit in the eastern margin of the NCC exhibits an alteration zonation of increasing K-feldspar alteration and subsequently increasing SQP alteration from the unaltered hosting granite towards orebodies. Trace element and Li isotopic compositions of unaltered, K-feldspar-altered, and SQP-altered granites, integrated with in-situ oxygen isotopic compositions of quartz from different
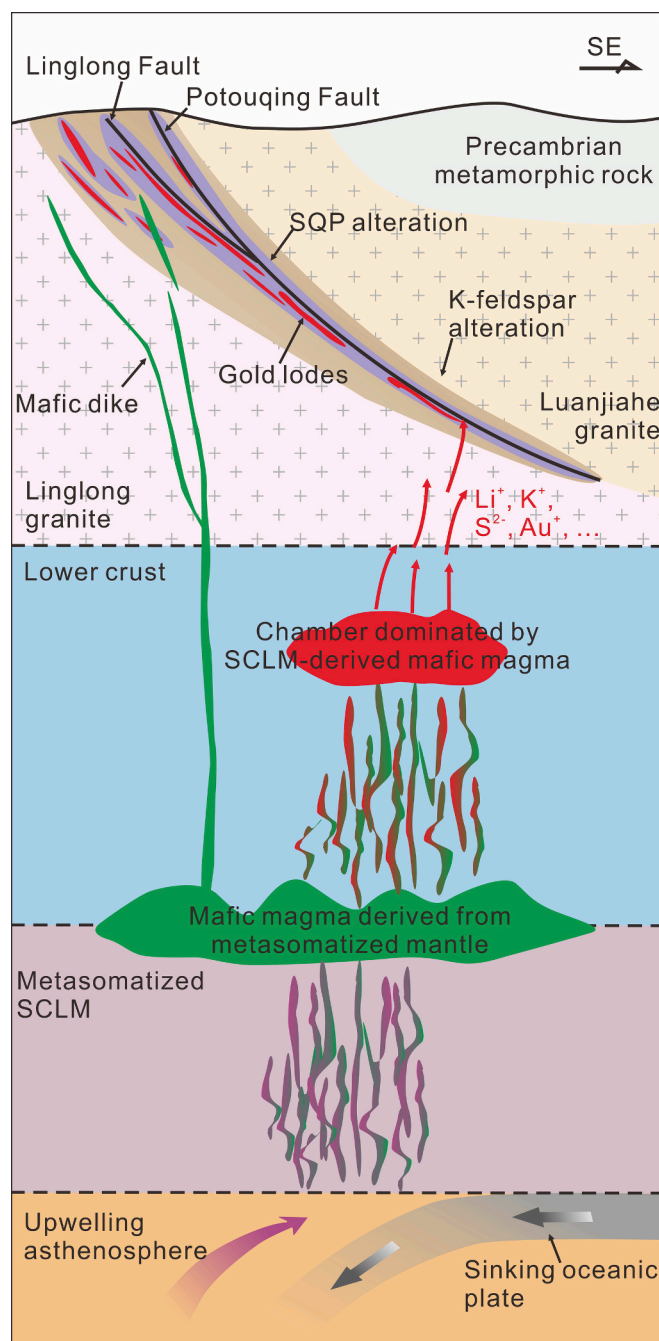

Fig. 9. Cartoon illustrating the hydrothermal alteration and associated gold mineralization at the Linglong gold deposit (modified from Li et al., 2023). Not to scale and see details in the text. (For interpretation of the references to colour in this figure legend, the reader is referred to the web version of this article.)

stages, suggest that fluids responsible for the K-feldspar and SQP alteration were predominantly sourced from the metasomatized lithospheric mantle-derived mafic magmas. The Li isotopic variation during the K-feldspar alteration was controlled by Rayleigh fractionation, whereas further reaction and buffering with the ore fluids accounted for the Li isotopic variations of SQP alteration zones and the associated gold mineralization. This study highlights that Li and in-situ oxygen isotopes are effective tools in tracing the source of hydrothermal fluids and fluid-rock interactions.

Declaration of Competing Interest

The authors declare that they have no known competing financial interests or personal relationships that could have appeared to influence the work reported in this paper.

Data availability

Data will be made available on request.

Acknowledgments

Appendix A. Supplementary material

Supplementary data to this article can be found online at https://doi.org/10.1016/j.chemgeo.2023.121696.

References

Baertschi, P., 1976. Absolute ^{18}O content of standard mean ocean water. Earth Planet. Sci. Lett. 31, 341–344.

Bao, C., Chen, B., Liu, C., Zheng, J., Liu, S., 2021. Lithium isotopic systematics of ore-forming fluid in the orogenic gold deposits, Jiaodong Peninsula (East China): Implications for ore-forming mechanism. Ore Geol. Rev. 136, 104254.

Bea, F., Pereira, M.D., Stroh, A., 1994. Mineral/leucosome trace-element partitioning in a peraluminous migmatite (a laser ablation-ICP-MS study). Chem. Geol. 117, 291–312.

Bernal, N.F., Gleeson, S.A., Dean, A.S., Liu, X., Hoskin, P., 2014. The source of halogens in geothermal fluids from the Taupo Volcanic Zone, North Island, New Zealand. Geochim. Cosmochim. Ac. 126, 265–283.

Bottinga, Y., Javoy, M., 1973. Comments on oxygen isotope geothermometry. Earth Planet. Sci. Lett. 20, 250–265.

Bottomley, D.J., Chan, L.H., Katz, A., Starinsky, A., Clark, I.D., 2003. Lithium isotope geochemistry and origin of Canadian Shield Brines. Groundwater. 41, 847–856.

Brant, C., Coogan, L.A., Gillis, K.M., Seyfried, W.E., Pester, N.J., Spence, J., 2012. Lithium and Li-isotopes in young altered upper oceanic crust from the East Pacific rise. Geochim. Cosmochim. Ac. 96, 272–293.

Bryant, C.J., Chappell, B.W., Bennett, V.C., McCulloch, M.T., 2004. Lithium isotopic compositions of the New England Batholith: correlations with inferred source rock compositions. Earth Env. Sci. T. R. So. 95, 199–214.

Burrows, D.R., Wood, P.C., Spooner, E.T.C., 1986. Carbon isotope evidence for a magmatic origin for Archaean gold-quartz vein ore deposits. Nature. 321, 851–854.

Chan, L.H., Edmond, J.M., Thompson, G., Gillis, K., 1992. Lithium isotopic composition of submarine basalts: implications for the lithium cycle in the oceans. Earth Planet. Sci. Lett. 108, 151–160.

Chan, L.H., Edmond, J.M., Thompson, G., 1993. A lithium isotope study of hot springs and metabasalts from mid-ocean ridge hydrothermal systems. J. Geophys. Res. 98, 9653–9659.

Chan, L.H., Leeman, W.P., Plank, T., 2006. Lithium isotopic composition of marine sediments. Geochem. Geophys. Geosyst. 7, Q06005.

Chen, J.F., Xie, Z., Li, H.M., Zhang, D., Zhou, T.X., Park, Y.S., Ahn, K.S., Chen, D.G., Zhang, X., 2003. U-Pb zircon ages for a collision-related K-rich complex at Shidao in the Sulu ultrahigh pressure terrane, China. Geochem. J. 37, 35–46.

Chi, G.X., Lu, H.Z., 2008. Validation and representation of fluid inclusion microthermometric data using the fluid inclusion assemblage (FIA) concept. Acta Petrol. Sin. 24, 1945–1953 (in Chinese with English abstract).

Chi, G.X., Diamond, L.W., Lu, H.Z., Lai, J.Q., Chu, H.X., 2021. Common problems and pitfalls in fluid inclusion study: a review and discussion. Minerals. 11, 7.

Coplen, T.B., Kendall, C., Hopple, J., 1983. Comparison of stable isotope reference samples. Nature. 302, 236–238.

Deng, J., Wang, C.M., Bagas, L., Carranza, E.J.M., Lu, Y.J., 2015. Cretaceous-Cenozoic tectonic history of the Jiaojia Fault and gold mineralization in the Jiaodong Peninsula, China: constraints from zircon U-Pb, illite K-Ar, and apatite fission track thermochronometry. Mineral. Deposita 50, 987–1006.

Deng, J., Wang, Q.F., Santosh, M., Liu, X.F., Liang, Y.Y., Yang, L.Q., Zhao, R., Yang, L., 2020a. Remobilization of metasomatized mantle lithosphere: a new model for the Jiaodong gold province, eastern China. Mineral. Deposita 55, 257–274.

Deng, J., Qiu, K.F., Wang, Q.F., Goldfarb, R., Yang, L.Q., Zi, J.W., Geng, J.Z., Ma, Y., 2020b. In situ dating of hydrothermal monazite and implications for the geodynamic controls on ore formation in the Jiaodong gold province, eastern China. Econ. Geol. 115, 671–685.

Fan, H.R., Lan, T.G., Li, X.H., Santosh, M., Yang, K.F., Hu, F.F., Feng, K., Hu, H.L., Peng, H.W., Zhang, Y.W., 2021. Conditions and processes leading to large-scale gold deposition in the Jiaodong province, eastern China. Sci. China Earth Sci. 64, 1504–1523.

Fan, G.H., Li, J.W., Valley, J.W., Scicchitano, M.R., Brown, P.E., Yang, J.H., Robinson, P.T., Deng, X.D., Wu, Y.F., Li, Z.K., Gao, W.S., Li, S.Y., Zhao, S.R., 2022. Garnet secondary ion mass spectrometry oxygen isotopes reveal crucial roles of pulsed magmatic fluid and its mixing with meteoric water in lode gold genesis. Proc. Natl. Acad. Sci. 119, e2116380119.

Fekete, S., Weis, P., Driesner, T., Bouvier, A., Baumgartner, L., Heinrich, C.A., 2016. Contrasting hydrological processes of meteoric water incursion during magmatic-hydrothermal ore deposition: an oxygen isotope study by ion microprobe. Earth Planet. Sci. Lett. 451, 263–271.

Feng, K., Fan, H.R., Groves, D.I., Yang, K.F., Hu, F.F., Liu, X., Cai, Y.C., 2020. Geochronological and sulfur isotopic evidence for the genesis of the post-magmatic, deeply sourced, and anomalously gold-rich Daliuhang orogenic deposit, Jiaodong, China. Mineral. Deposita 55, 293–308.

Fourny, A., Weis, D., Scoates, J.S., 2016. Comprehensive Pb-Sr-Nd-Hf isotopic, trace element, and mineralogical characterization of mafic to ultramafic rock reference materials. Geochem. Geophys. Geosyst. 17, 739–773.

Frimmel, H.E., 2008. Earth's continental crustal gold endowment. Earth Planet. Sci. Lett. 267, 45–55.

Gao, S., Hofstra, A.H., Zou, X.Y., Valley, J.W., Kitajima, K., Marsh, E.E., Lowers, H.A., Adams, D.T., Qin, K.Z., Xu, H., 2021. Oxygen isotope evidence for input of magmatic fluids and precipitation of Au-Ag-tellurides in an otherwise ordinary adularia-sericite epithermal system in NE China. Am. Mineral. 106, 2003–2019.

Goldfarb, R.J., Groves, D.I., 2015. Orogenic gold: Common or evolving fluid and metal sources through time. Lithos. 233, 2–26.

Goldfarb, R.J., Baker, T., Dube, B., Groves, D.I., Hart, C.J., Gosselin, P., 2005. Distribution, character, and genesis of gold deposits in metamorphic terranes. Econ. Geol. 100th Anniversary Volume, 407–450.

Goldfarb, R.J., Hart, C., Davis, G., Groves, D., 2007. East Asian gold: deciphering the anomaly of Phanerozoic gold in Precambrian cratons. Econ. Geol. 102, 341–345.

Goldstein, R.H., Reynolds, T.J., 1994. Systematics of fluid inclusions in diagenetic minerals. SEPM Short Course. 31, 1–199.

Groves, D.I., Goldfarb, R.J., Gebre-Mariam, M., Hagemann, S.G., Robert, F., 1998. Orogenic gold deposits: a proposed classification in the context of their crustal distribution and relationship to other gold deposit types. Ore Geol. Rev. 13, 7–27.

Groves, D.I., Santosh, M., Deng, J., Wang, Q.F., Yang, L.Q., Zhang, L., 2020. A holistic model for the origin of orogenic gold deposits and its implications for exploration. Mineral. Deposita 55, 275–292.

Guo, L.N., Deng, J., Yang, L.Q., Wang, Z.L., Wang, S.R., Wei, Y.J., Chen, B.H., 2020. Gold deposition and resource potential of the Linglong gold deposit, Jiaodong Peninsula: Geochemical comparison of ore fluids. Ore Geol. Rev. 120, 103434.

Haroldson, E.L., Brown, P.E., Ishida, A., Valley, J.W., 2020. SIMS oxygen isotopes indicate Phanerozoic fluids permeated a Precambrian gold deposit. Chem. Geol. 533, 119429.

Herzberg, C.T., Fyfe, W.S., Carr, M.J., 1983. Density constraints on the formation of the continental Moho and crust. Contrib. Mineral. Petrol. 84, 1–5.

Hoover, W.F., Penniston-Dorland, S.C., Baumgartner, L.P., Bouvier, A.S., Baker, D., Dragovic, B., Gion, A., 2021. A method for secondary ion mass spectrometry measurement of lithium isotopes in garnet: the utility of glass reference materials. Geostand. Geoanal. Res. 45, 477–499.

Icenhower, J., London, D., 1995. An experimental study of element partitioning among biotite, muscovite, and coexisting peraluminous silicic melt at 200 MPa (H$_2$O). Am. Mineral. 80, 1229–1251.

Large, R.R., Bull, S.W., Maslennikov, V.V., 2011. A carbonaceous sedimentary source-rock model for Carlin-type and orogenic gold deposits. Econ. Geol. 106, 331–358.

Li, J.W., Vasconcelos, P.M., Zhang, J., Zhou, M.F., Zhang, X.J., Yang, F.H., 2003. ^{40}Ar/^{39}Ar constraints on a temporal link between gold mineralization, magmatism, and continental margin transtension in the Jiaodong gold province, Eastern China. J. Geol. 111, 741–751.

Li, J.W., Vasconcelos, P.M., Zhou, M.F., Zhao, X.F., Ma, C.Q., 2006. Geochronology of the Pengjiakuang and Rushan gold deposits, eastern Jiaodong Gold Province, northeastern China: Implications for regional mineralization and geodynamic setting. Econ. Geol. 101, 1023–1038.

Li, J.W., Bi, S.J., Selby, D., Chen, L., Vasconcelos, P.M., Thiede, D., Zhou, M.F., Zhao, X.F., Li, Z.K., Qiu, H.N., 2012. Giant Mesozoic gold provinces related to the destruction of the North China craton. Earth Planet. Sci. Lett. 349-350, 26–37.

Li, X.H., Tang, G.Q., Gong, B., Yang, Y.H., Hou, K.J., Hu, Z.C., Li, Q.L., Liu, Y., Li, W.X., 2013. Qinghu zircon: a working reference for microbeam analysis of U-Pb age and Hf and O isotopes. Chin. Sci. Bull. 58, 4647–4654.

Li, J., Huang, X.L., Wei, G.J., Liu, Y., Ma, J.L., Han, L., He, P.L., 2018a. Lithium isotope fractionation during magmatic differentiation and hydrothermal processes in rare-metal granites. Geochim. Cosmochim. Ac. 240, 64–79.

Li, Y., Li, X.H., Selby, D., Li, J.W., 2018b. Pulsed magmatic fluid release for the formation of porphyry deposits: Tracing fluid evolution in absolute time from the Tibetan Qulong Cu-Mo deposit. Geology. 46, 7–10.

Li, X.H., Fan, H.R., Hu, F.F., Hollings, P., Yang, K.F., Liu, X., 2019. Linking lithospheric thinning and magmatic evolution of late Jurassic to early cretaceous granitoids in the Jiaobei Terrane, southeastern North China Craton. Lithos. 324-325, 280–296.

Li, X.H., Fan, H.R., Zhu, R.X., Steele-MacInnis, M., Yang, K.F., Liu, C.J., 2022. Texture, geochemistry, and geochronology of titanite and pyrite: Fingerprint of magmatic-hydrothermal fertile fluids in the Jiaodong au province. Am. Mineral. 107, 206–220.

Li, Z.K., Li, J.W., Sun, H.S., Zhao, X.F., Tomkins, A.G., Selby, D., Robinson, P.T., Deng, X. D., Wang, Z.C., Yuan, Z.Z., Zhao, S.R., 2023. Gold mineralized diorite beneath the Linglong ore field, North China Craton: New insights into the origin of decratonization-related gold deposits. Geol. Soc. Am. Bull. https://doi.org/10.1130/B36658.1.

Lin, Z.W., Zhao, X.F., Xiong, L., Zhu, Z.X., 2019. In-situ trace element analysis characteristics of pyrite in Sanshandao gold deposit in Jiaodong Peninsula: Implications for ore genesis. Adv. Earth Sci. 34, 399–413 (in Chinese with English abstract).

Liu, X.Y., Tan, J., He, H.Y., Gan, J.R., 2021. Origin of the Tudui-Shawang gold deposit, Jiaodong Peninsula, North China Craton: Constraints from fluid inclusion and H-O-He-Ar-S-Pb isotopic compositions. Ore Geol. Rev. 133, 104125.

Liu, S.J., Chen, B., Zheng, J.H., Sun, Y., Bao, C., Zhao, G.C., 2022. Lithium isotopic behaviour during high-temperature fluid-rock reactions of metapelites (>200 °C): a case study from the Baiyun orogenic gold deposit, Liaodong Peninsula, North China Craton. Chem. Geol. 611, 121121.

London, D., Hervig, R.L., Morgan, G.B., 1988. Melt-vapor solubilities and elemental partitioning in peraluminous granite-pegmatite systems: experimental results with Macusani glass at 200 MPa. Contrib. Mineral. Petrol. 99, 360–373.

Lu, Y.G., Xiao, Y.L., Nadeau, O., Yang, X.Y., Wang, Y.Y., Hou, Z.H., Sun, H., Li, D.Y., Gu, H.O., Deng, J.H., Tong, F.T., Tan, D.B., Qi, H.S., Ibrahim Bute, S., 2021. Inherited source affinity of Li and Hf isotopes for porphyry copper deposits from subduction and collisional settings. Ore Geol. Rev. 138, 104328.

Ma, L., Jiang, S., Hofmann, A.W., Dai, B., Hou, M., Zhao, K., Chen, L., Li, J., Jiang, Y., 2014. Lithospheric and asthenospheric sources of lamprophyres in the Jiaodong Peninsula: a consequence of rapid lithospheric thinning beneath the North China Craton? Geochim. Cosmochim. Ac. 124, 250–271.

Magna, T., Janoušek, V., Kohút, M., Oberli, F., Wiechert, U., 2010. Fingerprinting sources of orogenic plutonic rocks from Variscan belt with lithium isotopes and possible link to subduction-related origin of some A-type granites. Chem. Geol. 274, 94–107.

Mao, J.W., Li, H.M., Wang, Y.T., Zhang, C.Q., Wang, R.T., 2005. The relationship between mantle-derived fluid and gold ore-formation in the Eastern Shandong Peninsula: evidence from D-O-C-S isotopes. Acta Geol. Sin. 79, 839–857 (in Chinese with English abstract).

Marks, M.A., Rudnick, R.L., Ludwig, T., Marschall, H., Zack, T., Halama, R., McDonough, W.F., Rost, D., Wenzel, T., Vicenzi, E.P., 2008. Sodic pyroxene and sodicamphibole as potential reference materials for in situ lithium isotope determinations by SIMS. Geostand. Geoanal. Res. 32, 295–310.

Marschall, H.R., Pogge von Strandmann, P.A.E., Seitz, H., Elliott, T., Niu, Y., 2007. The lithium isotopic composition of orogenic eclogites and deep subducted slabs. Earth Planet. Sci. Lett. 262, 563–580.

Marschall, H.R., Wanless, V.D., Shimizu, N., Pogge von Strandmann, P.A.E., Elliott, T., Monteleone, B.D., 2017. The boron and lithium isotopic composition of mid-ocean ridge basalts and the mantle. Geochim. Cosmochim. Ac. 207, 102–138.

Martin, C., Ponzevera, E., Harlow, G., 2015. In situ lithium and boron isotope determinations in mica, pyroxene, and serpentine by LA-MC-ICP-MS. Chem. Geol. 412, 107–116.

Millot, R., Guerrot, C., Vigier, N., 2004. Accurate and high-precision measurement of lithium isotopes in two reference materials by MC-ICP-MS. Geostand. Geoanal. Res. 28, 153–159.

Muntean, J.L., Cline, J.S., Simon, A.C., Longo, A.A., 2011. Magmatic-hydrothermal origin of Nevada's Carlin-type gold deposits. Nat. Geosci. 4, 122–127.

Nadeau, O., Voinot, A., Leybourne, M., 2021. Lithium isotopes at gold deposits: Insights from the giant Kirkland Lake gold deposit, Canada. Precambrian Res. 362, 106308.

Nishio, Y., Nakai, S.I., Yamamoto, J., Sumino, H., Matsumoto, T., Prikhod Ko, V.S., Arai, S., 2004. Lithium isotopic systematics of the mantle-derived ultramafic xenoliths: implications for EM1 origin. Earth Planet. Sci. Lett. 217, 245–261.

Patten, C.G.C., Pitcairn, I.K., Molnár, F., Kolb, J., Beaudoin, G., Guilmette, C., Peillod, A., 2020. Gold mobilization during metamorphic devolatilization of Archean and Paleoproterozoic metavolcanic rocks. Geology. 48, 1110–1114.

Pei, F.P., Xu, W.L., Wang, Q.H., Wang, D.Y., Lin, J.Q., 2004. Mesozoic basalt and mineral chemistry of the mantle-derived xenocrysts in Feixian, western Shandong, China: constraints on nature of Mesozoic lithospheric mantle. Geol. J. China Univ. 10, 88–97 (in Chinese with English abstract).

Penniston-Dorland, S., Bebout, G.E., Pogge Von Strandmann, P.A.E., Elliott, T., Sorensen, S.S., 2012. Lithium and its isotopes as tracers of subduction zone fluids and metasomatic processes: evidence from the Catalina Schist, California, USA. Geochim. Cosmochim. Ac. 77, 530–545.

Penniston-Dorland, S., Liu, X.M., Rudnick, R.L., 2017. Lithium isotope geochemistry. Rev. Mineral. Geochem. 82, 165–217.

Phillips, G.N., Powell, R., 2010. Formation of gold deposits: a metamorphic devolatilization model. J. Metamorph. Geol. 28, 689–718.

Pitcairn, I.K., Leventis, N., Beaudoin, G., Faure, S., Guilmette, C., Dubé, B., 2021. A metasedimentary source of gold in Archean orogenic gold deposits. Geology. 49, 862–866.

Qi, L., Grégoire, D.C., 2000. Determination of trace elements in twenty six Chinese geochemistry reference materials by inductively coupled plasma-mass spectrometry. Geostand. Newslett. 24, 51–63.

Qiu, L., Rudnick, R.L., McDonough, W.F., Bea, F., 2011. The behavior of lithium in amphibolite- to granulite-facies rocks of the Ivrea-Verbano Zone, NW Italy. Chem. Geol. 289, 76–85.

Roedder, E., 1984. Fluid inclusions. Rev. Mineral. 12, 1–646.

Romer, R.L., Meixner, A., Förster, H., 2014. Lithium and boron in late-orogenic granites – Isotopic fingerprints for the source of crustal melts? Geochim. Cosmochim. Ac. 131, 98–114.

Romer, R.L., Förster, H., Glodny, J., 2022. Role of fractional crystallization, fluid-melt separation, and alteration on the Li and B isotopic composition of a highly evolved composite granite pluton: the case of the Eibenstock granite, Erzgebirge, Germany. Lithos. 422-423, 106722.

Rudnick, R.L., Tomascak, P.B., Njo, H.B., Gardner, L.R., 2004. Extreme lithium isotopic fractionation during continental weathering revealed in saprolites from South Carolina. Chem. Geol. 212, 45–57.

Sai, S.X., Zhao, T.M., Wang, Z.L., Huang, S.Y., Zhang, L., 2016. Petrogenesis of Linglong biotite granite: Constraints from mineralogical characteristics. Acta Petrol. Sin. 32, 2477–2496 (in Chinese with English abstract).

Schuessler, J.A., Schoenberg, R., Sigmarsson, O., 2009. Iron and lithium isotope systematics of the Hekla volcano, Iceland — evidence for Fe isotope fractionation during magma differentiation. Chem. Geol. 258, 78–91.

Sharp, Z.D., Gibbons, J.A., Maltsen, O., Atudorei, V., Pack, A., Sengupta, S., Shock, E.L., Knauth, L.P., 2016. A calibration of the triple oxygen isotope fractionation in the SiO₂-H₂O system and applications to natural samples. Geochim. Cosmochim. Ac. 186, 105–119.

Song, M.C., Yang, L.Q., Fan, H.R., Yu, X.F., Ding, Z.J., Zhang, Y.W., Qiu, K.F., Li, J., Zhang, L., Wang, B., Li, S.Y., 2022. Current progress of metallogenic research and deep prospecting of gold deposits in the Jiaodong Peniusula during 10 years for Exploration Breakthrough Strategic Action. Geol. Bull. China. 41, 903–935 (in Chinese with English abstract).

Steadman, J.A., Large, R.R., 2016. Synsedimentary, diagenetic, and metamorphic pyrite, pyrrhotite, and marcasite at the Homestake BIF-hosted gold deposit, South Dakota, USA: Insights on Au-as ore genesis from textural and LA-ICP-MS trace element studies. Econ. Geol. 111, 1731–1752.

Steinmann, L.K., Oeser, M., Horn, I., Seitz, H.M., Weyer, S., 2019. In situ high-precision lithium isotope analyses at low concentration levels with femtosecond-LA-MC-ICP-MS. J. Anal. At. Spectrom. 34, 1447–1458.

Tan, J., Wei, J., Audétat, A., Pettke, T., 2012. Source of metals in the Guocheng gold deposit, Jiaodong Peninsula, North China Craton: link to early cretaceous mafic magmatism originating from Paleoproterozoic metasomatized lithospheric mantle. Ore Geol. Rev. 48, 70–87.

Tan, J., Wei, J.H., He, H.Y., Su, F., Li, Y.J., Fu, L.B., Zhao, S.Q., Xiao, G.L., Zhang, F., Xu, J.F., Liu, Y., Stuart, F.M., Zhu, R.X., 2018. Noble gases in pyrites from the Guocheng-Liaoshang gold belt in the Jiaodong province: evidence for a mantle source of gold. Chem. Geol. 480, 105–115.

Tang, Y.J., Zhang, H.F., Ying, J.F., 2007. Review of the lithium isotope system as a geochemical tracer. Int. Geol. Rev. 49, 374–388.

Tang, Y.J., Zhang, H.F., Ying, J.F., 2009. Discussion on fractionation mechanism of lithium isotopes. Earth Sci.-J. China Univ. Geosci. 34, 43–55 (in Chinese with English abstract).

Tanner, D., Henley, R.W., Mavrogenes, J.A., Holden, P., 2013. Combining in situ isotopic, trace element and textural analyses of quartz from four magmatic-hydrothermal ore deposits. Contrib. Mineral. Petrol. 166, 1119–1142.

Taylor, H.P., 1974. The application of oxygen and hydrogen isotope studies to problems of hydrothermal, alteration and ore deposition. Econ. Geol. 69, 843–883.

Teng, F.Z., McDonough, W.F., Rudnick, R.L., Walker, R.J., 2006. Diffusion-driven extreme lithium isotopic fractionation in country rocks of the Tin Mountain pegmatite. Earth Planet. Sci. Lett. 243, 701–710.

Tomascak, P.B., 2004. Developments in the understanding and application of lithium isotopes in the earth and planetary sciences. Rev. Mineral. Geochem. 55, 153–195.

Tomascak, P.B., Tera, F., Helz, R.T., Walker, R.J., 1999. The absence of lithium isotope fractionation during basalt differentiation; new measurements by multicollector sector ICP-MS. Geochim. Cosmochim. Ac. 63, 907–910.

Tomascak, P.B., Langmuir, C.H., le Roux, P.J., Shirey, S.B., 2008. Lithium isotopes in global mid-ocean ridge basalts. Geochim. Cosmochim. Ac. 72, 1626–1637.

Tomkins, A.G., 2010. Windows of metamorphic sulfur liberation in the crust: Implications for gold deposit genesis. Geochim. Cosmochim. Ac. 74, 3246–3259.

Valley, J.W., Graham, C.M., 1991. Ion microprobe analysis of oxygen isotope ratios in granulite facies magnetites: diffusive exchange as a guide to cooling history. Contrib. Mineral. Petrol. 109, 38–52.

Vigier, N., Rollion-Bard, C., Spezzaferri, S., Brunet, F., 2007. In situ measurements of Li isotopes in foraminifera. Geochem. Geophys. Geosyst. 8, Q01003.

Wang, H., 2021. Reddish alteration processes and its contribution to gold mineralization in Sizhuang gold deposit, northwestern Jiaodong Peninsula. China Univ. Geosci. (Beijing) 1–64 (in Chinese with English abstract).

Wang, Z.L., Yang, L.Q., Deng, J., Santosh, M., Zhang, H.F., Liu, Y., Li, R.H., Huang, T., Zheng, X.L., Zhao, H., 2014. Gold-hosting high Ba-Sr granitoids in the Xincheng gold deposit, Jiaodong Peninsula, East China: Petrogenesis and tectonic setting. J. Asian Earth Sci. 95, 274–299.

Wang, Z.C., Cheng, H., Zong, K.Q., Geng, X.L., Liu, Y.S., Yang, J.H., Wu, F.Y., Becker, H., Foley, S., Wang, C.Y., 2020. Metasomatized lithospheric mantle for Mesozoic giant gold deposits in the North China craton. Geology. 48, 169–173.

Wang, X., Wang, Z.C., Cheng, H., Zong, K.Q., Wang, C.Y., Ma, L., Cai, Y.C., Foley, S., Hu, Z.C., 2022a. Gold endowment of the metasomatized lithospheric mantle for giant gold deposits: Insights from lamprophyre dykes. Geochim. Cosmochim. Ac. 316, 21–40.

Wang, Q.F., Yang, L., Zhao, H.S., Groves, D.I., Weng, W.J., Xue, S.C., Li, H.J., Dong, C.Y., Yang, L.Q., Li, D.P., Deng, J., 2022b. Towards a universal model for orogenic gold systems: a perspective based on Chinese examples with geodynamic, temporal, and deposit-scale structural and geochemical diversity. Earth-Sci. Rev. 224, 103861.

Wei, C.J., Zheng, Y.F., 2020. Metamorphism, fluid behavior and magmatism in oceanic subduction zones. Sci. China Earth Sci. 63, 52–77.

Wen, B.J., Fan, H.R., Santosh, M., Hu, F.F., Pirajno, F., Yang, K.F., 2015. Genesis of two different types of gold mineralization in the Linglong gold field, China: Constrains from geology, fluid inclusions and stable isotope. Ore Geol. Rev. 65, 643–658.

Wen, B.J., Fan, H.R., Hu, F.F., Liu, X., Yang, K.F., Sun, Z.F., Sun, Z.F., 2016. Fluid evolution and ore genesis of the giant Sanshandao gold deposit, Jiaodong gold province, China: Constrains from geology, fluid inclusions and H-O-S-He-Ar isotopic compositions. J. Geochem. Explor. 171, 96–112.

Wu, F.Y., Yang, J.H., Xu, Y.G., Wilde, S.A., Walker, R.J., 2019. Destruction of the North China Craton in the Mesozoic. Annu. Rev. Earth Planet. Sci. 47, 173–195.

Wunder, B., Meixner, A., Romer, R.L., Heinrich, W., 2006. Temperature-dependent isotopic fractionation of lithium between clinopyroxene and high-pressure hydrous fluids. Contrib. Mineral. Petrol. 151, 112–120.

Wunder, B., Meixner, A., Romer, R.L., Feenstra, A., Schettler, G., Heinrich, W., 2007. Lithium isotope fractionation between Li-bearing staurolite, Li-mica and aqueous fluids: an experimental study. Chem. Geol. 238, 277–290.

Xavier, R.P., Foster, R.P., 1999. Fluid evolution and chemical controls in the Fazenda Maria Preta (FMP) gold deposit, Rio Itapicuru Greenstone Belt, Bahia, Brazil. Chem. Geol. 154, 133–154.

Xie, S.W., Wu, Y.B., Zhang, Z.M., Qin, Y.C., Liu, X.C., Wang, H., Qin, Z.W., Liu, Q., Yang, S.H., 2012. U-Pb ages and trace elements of detrital zircons from early cretaceous sedimentary rocks in the Jiaolai Basin, north margin of the Sulu UHP terrane: Provenances and tectonic implications. Lithos 154, 346–360.

Xiong, L., Zhao, X.F., Zhao, S.R., Lin, H.T., Lin, Z.W., Zhu, Z.X., Wang, Z.C., Li, M.Y.H., Li, J.W., 2021. Formation of giant gold provinces by subduction-induced reactivation of fossilized, metasomatized continental lithospheric mantle in the North China Craton. Chem. Geol. 580, 120362.

Xu, L., Luo, C., Wen, H., 2019. A revisited purification of Li for 'Na breakthrough' and its isotopic determination by MC-ICP-MS. Geostand. Geoanal. Res. 44, 201–214.

Xu, R., Romer, R.L., Glodny, J., 2021. External fluids cause alteration and metal redistribution in the granite-hosted Tangziwa Sn-Cu deposit, Gejiu district, China. Lithos. 382-383, 105937.

Xue, Y.X., Campbell, I., Ireland, T.R., Holden, P., Armstrong, R., 2013a. No mass-independent sulfur isotope fractionation in auriferous fluids supports a magmatic origin for Archean gold deposits. Geology. 41, 791–794.

Xue, J.L., Li, S.R., Sun, W.Y., Zhang, Y.Q., Zhang, X., Liu, C.L., 2013b. Helium and argon isotopic composition in fluid inclusions and the source of ore-forming materials of Denggezhuang gold deposit in Jiaodong Peninsula. J. Jilin Univ. (Earth Sci. Ed.) 43, 400–414 (in Chinese with English abstract).

Yang, J.H., Zhou, X.H., 2001. Rb-Sr, Sm-Nd, and Pb isotope systematics of pyrite: Implications for the age and genesis of lode gold deposits. Geology. 29, 711–714.

Yang, J.H., Chung, S.L., Wilde, S.A., Wu, F.Y., Chu, M.F., Lo, C.H., Fan, H.R., 2005. Petrogenesis of post-orogenic syenites in the Sulu Orogenic Belt, East China:

geochronological, geochemical and Nd-Sr isotopic evidence. Chem. Geol. 214, 99–125.

Yang, L.Q., Deng, J., Guo, L.N., Wang, Z.L., Li, X.Z., Li, J.L., 2016. Origin and evolution of ore fluid, and gold-deposition processes at the giant Taishang gold deposit, Jiaodong Peninsula, eastern China. Ore Geol. Rev. 72, 585–602.

Yang, Y., Wang, X.X., Yu, X.W., Ke, C.H., Wang, L.G., Guo, R.P., Wang, S.A., Li, X.X., 2017. Chemical composition of biotite and amphibole from Mesozoic granites in northwestern Jiaodong Peninsula, China, and their implications. Acta Petrol. Sin. 33, 3123–3136 (in Chinese with English abstract).

Yang, Q., Xia, X.P., Zhang, W.F., Zhang, Y.Q., Xiong, B.Q., Xu, Y.G., Wang, Q., Wei, G.J., 2018. An evaluation of precision and accuracy of SIMS oxygen isotope analysis. Solid Earth Sci. 3, 81–86.

Yang, J.H., Xu, L., Sun, J.F., Zeng, Q.D., Zhao, Y.N., Wang, H., Zhu, Y.S., 2021. Geodynamic of decratonization and related magmatism and mineralization in the North China Craton. Sci. China Earth Sci. 64, 1409–1427.

Zhang, L.G., Chen, Z.S., Liu, J.X., Yu, G.X., Wang, K.F., Wang, B.C., Xu, J.F., Zheng, W.S., Li, D.Y., Li, H., Hou, D.Y., 1995. Two-Stage Water-Rock Isotopic Exchange Theory and Implied on Prospecting. Geological Publishing House, Beijing (in Chinese).

Zhang, H.F., Sun, M., Zhou, X.H., Fan, W.M., Zhai, M.G., Yin, J.F., 2002. Mesozoic lithosphere destruction beneath the North China Craton: evidence from major-, trace-element and Sr-Nd-Pb isotope studies of Fangcheng basalts. Contrib. Mineral. Petrol. 144, 241–254.

Zhang, B.L., Shan, W., Li, D.P., Xiao, B.J., Wang, Z.L., Zhang, R.Z., 2017. Hydrothermal alteration in the Dayingezhuang gold deposit, Jiaodong, China. Acta Petrol. Sin. 33, 2256–2272 (in Chinese with English abstract).

Zhang, L., Weinberg, R.F., Yang, L.Q., Groves, D.I., Sai, S.X., Matchan, E., Phillips, D., Kohn, B.P., Miggins, D.P., Liu, Y., Deng, J., 2020. Mesozoic orogenic gold mineralization in the Jiaodong Peninsula, China: a focused event at 120 ± 2 Ma during cooling of pregold granite intrusions. Econ. Geol. 115, 415–441.

Zhao, G.C., Sun, M., Wilde, S.A., Li, S.Z., 2005. Late Archean to Paleoproterozoic evolution of the North China Craton: key issues revisited. Precambrian Res. 136, 177–202.

Zheng, Y.F., 1993. Calculation of oxygen isotope fractionation in hydroxyl-bearing silicates. Earth Planet. Sci. Lett. 120, 247–263.

Zhu, G., Niu, M.L., Xie, C.L., Wang, Y.S., 2010. Sinistral to normal faulting along the Tan-Lu fault zone: evidence for geodynamic switching of the East China continental margin. J. Geol. 118, 277–293.

Zhu, R.X., Chen, L., Wu, F.Y., Liu, J.L., 2011. Timing, scale and mechanism of the destruction of the North China Craton. Sci. China Earth Sci. 54, 789–797.

Zhu, R.X., Fan, H.R., Li, J.W., Meng, Q.R., Li, S.R., Zeng, Q.D., 2015. Decratonic gold deposits. Sci. China Earth Sci. 58, 1523–1537.

Zhu, Z.X., Zhao, X.F., Lin, Z.W., Zhao, S.R., 2020. In situ trace elements and sulfur isotope analysis of pyrite from Jinchiling gold deposit in the Jiaodong region: Implications for ore genesis. Earth Sci. 45, 945–959 (in Chinese with English abstract).